

1 **Largest aftershock nucleation driven by afterslip during the 2014 Iquique sequence**  
2  
3

4 **Yuji Itoh<sup>1,2,\*</sup>, Anne Socquet<sup>1</sup>, and Mathilde Radiguet<sup>1</sup>**

5  
6 <sup>1</sup>Univ. Grenoble Alpes, Univ. Savoie Mont Blanc, CNRS, IRD, Univ. Gustave Eiffel, ISTerre,  
7 38000 Grenoble, France.

8 <sup>2</sup>Earthquake Research Institute, The University of Tokyo, Tokyo, Japan.  
9

10 \*Corresponding author: Yuji Itoh ([yitoh@eri.u-tokyo.ac.jp](mailto:yitoh@eri.u-tokyo.ac.jp))  
11

12 **Key Points:**

- 13 • Global Positioning System captured crustal deformation during 27 hours between the  
14 2014 Iquique mainshock and its largest aftershock  
15 • The mainshock and the largest aftershock areas are separated by an aseismic area, likely  
16 preventing both from rupturing as a single event  
17 • The largest aftershock nucleation is a mixture of seismicity and decelerating afterslip,  
18 favoring a rate-dependent cascade-up model  
19

**20 Abstract (<= 150 words)**

21 Various earthquake models predict that aseismic slip modulates the seismic rupture process but  
22 actual observations of such seismic-aseismic interaction are scarce. We analyze seismic and  
23 aseismic processes during the 2014 Iquique earthquake sequence. High-rate Global Positioning  
24 System (GPS) displacements demonstrate that most of the early afterslip is located downdip of  
25 the M 8.1 mainshock and is accompanied by decaying aftershock activity. An intriguing  
26 secondary afterslip peak is located ~120 km south of the mainshock epicenter. The area of this  
27 secondary afterslip peak likely acted as a barrier to the propagating mainshock rupture and  
28 delayed the M 7.6 largest aftershock, which occurred 27 hours later. Interevent seismicity in this  
29 secondary afterslip area ended with a M 6.1 near the largest aftershock epicenter, kicking the  
30 largest aftershock rupture in the same area. Hence, the interevent afterslip likely promoted the  
31 largest aftershock nucleation by destabilizing its source area, favoring a rate-dependent cascade-  
32 up model.

33

**34 Plain Language Summary**

35 Subduction zone faults host both fast (regular earthquakes, seismic) and slow (aseismic) slip.  
36 Simulation models predict that slow slip can affect fast slip processes. We explored such an  
37 interaction taking place during the 2014 Iquique earthquake offshore northern Chile using  
38 observation data of crustal deformation by GPS and earthquakes. We discovered that the fast  
39 mainshock slip was terminated by a slowly slipping fault zone, which prevented the  
40 simultaneous occurrence of the largest aftershock. Furthermore, afterslip, one type of slow slip  
41 following the mainshock, helped the occurrence of the largest aftershock 27 hours after the  
42 mainshock. Therefore, the sequential occurrence of large earthquakes can be controlled by  
43 slowly slipping faults.

44

**45 1 Introduction**

46 Subduction zone megathrust faults host diverse slip behaviors. Seismic and aseismic slip  
47 are two complementary types (e.g., Scholz, 1998). Laboratory experiments and mechanical  
48 simulations of earthquake cycles demonstrate that aseismic and seismic processes commonly  
49 interact with each other in various manners. For example, the nucleation of numerical and  
50 laboratory earthquakes is associated with precursory seismic and aseismic processes (e.g.,  
51 Cattania & Segall, 2021; Dieterich, 1992; Marty et al., 2023; McLaskey, 2019; Noda et al.,  
52 2013). Such seismic and aseismic interaction processes are often observed associated with large  
53 earthquakes as well. Short-term (a few days; e.g., Kato et al., 2012; Ohta et al., 2012) and long-  
54 term (a few months to a decade; Ito et al., 2013; Marill et al., 2021; Mavrommatis et al., 2014;  
55 Yokota & Koketsu, 2015) changes in geodetic time series and seismic activity before the 2011  
56  $M_w$  9.0 Tohoku earthquake have been interpreted in this regard. In addition, seismic ruptures are  
57 often terminated by an aseismic segment (e.g., model; Kaneko et al., 2010, observations;  
58 Nishikawa et al., 2019; Perfettini et al., 2010; Rolandone et al., 2018). Finally, laboratory  
59 earthquakes can interact via migrating aseismic creep fronts, and thus be responsible for delayed  
60 triggering (e.g., Cebry et al., 2022). In nature, aftershock occurrence is often controlled by  
61 afterslip (Klein et al., 2021; Perfettini et al., 2018). These theoretical and observational studies

62 suggest that mechanically heterogeneous faults yield various scenarios of seismic-aseismic  
63 interactions.

64 The 2014 M 8.1 Iquique earthquake in northern Chile along the Nazca megathrust  
65 (Figure 1a) is also an excellent target for studying such seismic-aseismic interaction in nature.  
66 Long-term locking models illustrate a heterogeneous mosaic of locked and creeping areas  
67 (Jolivet et al., 2020; Li et al., 2015; Métois et al., 2016; Schurr et al., 2014). The 2014 event was  
68 preceded by short- (2-3 weeks) and long-term (8 months to years) precursory seismic and  
69 aseismic activities in and around the subsequent mainshock rupture area (Bedford et al., 2015;  
70 Boudin et al., 2022; Herman et al., 2016; Kato et al., 2016; Ruiz et al., 2014; Schurr et al., 2014;  
71 Socquet et al., 2017; Twardzik et al., 2022). Despite these previous studies, processes between  
72 the 2014 mainshock and the largest aftershock (M 7.6, Figure 1a), which we call “interevent” in  
73 this study, have so far remained unstudied. This largest aftershock occurred ~120 km south of  
74 the mainshock (Duputel et al., 2015; Hayes et al. 2014; Jara et al., 2018; Meng et al., 2015; Ruiz  
75 et al., 2014) and occurred 27 hours later. Resolving aseismic processes at such a short time scale  
76 is usually challenging because it requires high-rate GPS coordinates that are noisier than the  
77 standard daily coordinates. However, successful high-rate-GPS-based identification of early  
78 postseismic processes (e.g., Jiang et al., 2021; Liu et al., 2022; Miyazaki & Larson, 2008;  
79 Periollat et al. 2022; Tsang et al., 2019, Twardzik et al., 2021) suggest its applicability to the  
80 2014 Iquique case. This study investigates source processes during the 2014 Iquique sequence by  
81 unveiling the early postseismic slip for a few days using high-rate GPS and comparing them with  
82 seismicity. Then, we discuss their implications for earthquake mechanics, particularly the role of  
83 aseismic megathrust in rupture segmentation and nucleation of large earthquakes.

84

## 85 **2 Methods**

### 86 2.1 High-rate GPS data analysis

#### 87 2.1.1 GPS data cleaning

88 We employed 5-minute high-rate GPS coordinates processed by the Nevada Geodetic  
89 Laboratory (NGL; Blewitt et al., 2018; black in Figure S1). We removed coordinate fluctuations  
90 due to multipath (e.g., Bock et al., 2000; Itoh & Aoki, 2022; Ragheb et al., 2007) and diurnal  
91 variations using Seasonal-Trend decomposition using LOESS (STL) (Cleveland et al., 1990)  
92 with repeating periods of 23 hours and 55 minutes and 1 day, respectively (red and pink in  
93 Figure S1) from the 5-minute coordinate time series. Then, we removed common mode errors  
94 originating from fluctuations in the reference frame and satellite orbit errors (Wdowinski et al.,  
95 1997). We extracted common mode errors by stacking cleaned and despiked time series at 6 sites  
96 in the nodal direction of the mainshock and the largest aftershock, where little coseismic  
97 deformation is expected (Figure 1 and orange in Figure S1). We provide details of the cleaning  
98 procedure in Text S1.

99

#### 100 2.1.2 Computation of displacements at four stages

101 After correcting the time series for the common modes, we extracted displacements  
102 associated with the mainshock, the interevent stage, the largest aftershock, and the 2-day post-

103 largest-aftershock stages from these “cleaned” time series (blue in Figure S1). We fit a trajectory  
104 model (Figures 1c-e, S2a-c) between 5 days before and 30 days after the day of the mainshock.  
105 Our trajectory model consists of step and logarithmic terms (Equation (S2) in Text S2)  
106 representing coseismic static deformation and postseismic response assuming velocity-  
107 strengthening afterslip (Marone et al., 1991; Perfettini & Avouac, 2004; Perfettini et al., 2018),  
108 respectively. In the subsequent slip inversions, we used the cumulative displacements estimated  
109 using the trajectory model with time constants of the logarithmic term fitting fairly the “cleaned”  
110 data (Figures 1c-e, S2a-c; See Text S2 and Figures S3-S5 for details). Then, we computed a  
111 moving median of the time series without the co-seismic steps to extract the temporal evolution  
112 of the interevent displacements (Figure 2a; see Text S3 for details). As the moving median is  
113 non-parametric, it can keep more information from the original observations than the trajectory  
114 model predictions, which allows only for a monotonic change in the displacement (Figure S6).  
115 The window length of the median computation is 0.5 days. We obtained displacements during  
116 two interevent substages with an equal length (~13.5 hours) from the moving median time series.  
117

## 118 2.2 Slip inversions

119 We employed a non-linear slip inversion code SDM (Wang et al., 2009, 2013a) to infer  
120 slip distribution during the two earthquakes, the interevent and the post-largest-aftershock stages.  
121 This allows us to depict the interplay of seismic and aseismic slip in a methodologically  
122 consistent manner, despite many published coseismic models (Boudin et al., 2022; Duputel et al.,  
123 2015; Hayes et al. 2014; Jara et al., 2018; Meng et al., 2015; Ruiz et al., 2014). We inverted the  
124 three components of GPS displacements weighted according to their formal errors (See Text S4  
125 for details of interevent datasets). We used the homogeneous isotropic elastic half-space (Okada,  
126 1992) and Slab2 fault geometry (Figure 1a; Hayes, 2018). We imposed a slip roughness  
127 constraint to regularize the inversion problem and determined its strength using a trade-off curve  
128 of data misfit versus slip roughness (Figure S7-S8). We constrain the rake angle to be between  
129 45 and 135 degrees. We used 30 GPa for rigidity to compute seismic moment and Coulomb  
130 Stress Change (CSC; King et al. 1994; Figure S9; See Text S5). For the incremental slip during  
131 the two interevent substages (Figure 2e-f), we found it necessary to additionally constrain the  
132 upper bound of slip because the incremental displacements derived from the moving median  
133 analysis are noisier than the cumulative displacements derived from the trajectory model fit  
134 (details in Text S4). As presented below, the inferred slips have multiple peaks and an overlap of  
135 seismic and aseismic slips. Hence, we carried out several tests to assess the robustness of the  
136 inversion results (Figures S10-S13). Also, we used models with different roughness to grasp  
137 robust slip features (Figures S7-S8). In particular, rougher solutions likely highlight the  
138 “minimum” extent of the slipping area.

139

## 140 2.3 Seismicity analysis

141 We employed McBrearty et al. (2019)’s seismicity catalog which lists many moderate  
142 aftershocks (Figures 1b, 2e-g, and 3a) among available catalogs (Sippl et al., 2018; Soto et al.,  
143 2019a). We carried out analyses of seismicity count (Figure 2c) and seismic moment (Figure 2d)  
144 for two regions. We divided the target region at 20.2°S within a range from 71.5°W to 70.0°W to  
145 highlight the contrast in seismicity at the mainshock (labeled North) and the largest aftershock

146 (labeled South) latitudes. We computed the cumulative event count and seismic moment with a  
 147 0.002-day window. The seismic moment of each event is computed as  $10^{1.5M_L+9.1}$  where  $M_L$  is a  
 148 local magnitude from the catalog. The catalog we used tends to underestimate the magnitude of  
 149 large events, so we modified the magnitude of an event 45 minutes before the largest aftershock  
 150 from 5.6 to 6.1 for the moment computation (Soto et al., 2019a) (Table S1; Figure S14).  
 151

### 152 **3 Results**

#### 153 3.1 Cumulative geodetic slip distributions at each stage

154 The static cumulative displacements at each stage demonstrate a coherent trenchward  
 155 pattern (Figures 1 and S15), consistent with thrust faulting on the subduction interface (e.g., Jara  
 156 et al., 2018; Hoffmann et al., 2018; Shrivastava et al., 2019). The inferred two coseismic slip  
 157 patterns look similar to previous models which also used static offsets derived from high-rate  
 158 GPS data (Figure 3a; Jara et al., 2018). The imaged interevent cumulative geodetic slip has some  
 159 local maxima (blue contours in Figures 3a and S2e). The largest peak is located down-dip of the  
 160 mainshock slip, a typical feature due to the depth-dependent change in megathrust rheology (e.g.,  
 161 Scholz, 1998). Another well-resolved peak is located south of the mainshock slip peak at  
 162 seismogenic depth and is accompanied by moderate seismicity. One potentially missing slip  
 163 patch could be located up-dip of the mainshock peak slip where a cluster of moderate seismicity  
 164 is observed, some of which might be repeaters (Meng et al., 2015; Figures 4 and S16). Indeed, a  
 165 slip patch appears up-dip of the mainshock peak when the mainshock peak slip zone is masked in  
 166 the inversion (Figures S10c-d). Hence, an up-dip postseismic slip occurred, but it was not very  
 167 large, contrary to another postseismic observation following a similar magnitude earthquake  
 168 (e.g., Itoh et al., 2019; Miyazaki et al., 2004). The post-largest-aftershock geodetic slip has two  
 169 peaks at both the North and South subareas, representing a continuation of the mainshock-  
 170 induced postseismic slip superimposed with a postseismic slip enhanced by the largest aftershock  
 171 (greens contours in Figures 3 and S15i).

172 The geodetically determined moment contains the aseismic slip on the interface slip as  
 173 well as the seismic slip associated with aftershocks (e.g., Caballero et al., 2021; Twardzik et al.,  
 174 2021, 2022). Our seismicity analysis shows that seismic moments during the interevent and the  
 175 post-largest-aftershock stages are equivalent to  $M_w$  6.2 and 5.8, about 3% and 1% of the  
 176 corresponding geodetic moments  $M_w$  7.2 and 7.1, respectively (Table S1; Figure S14). Hence,  
 177 the early postseismic slip is substantially aseismic. This is much smaller than the early  
 178 postseismic deformation of the 2015 Illapel earthquake during 12 hours (Twardzik et al., 2021).  
 179 Seismic contributions at the North and South subareas are different and change with time (Table  
 180 S1 and Figure S14).

181 Then, the confirmed aseismic slip contribution in the interevent and the post-largest-  
 182 aftershock stages questions the overlap of the coseismic and aseismic slips (Figure 3a). This is  
 183 because their overlap contradicts the consensus based on the rate-and-state friction law (e.g.,  
 184 Scholz, 1998) and some observations (Nishikawa et al., 2019; Perfettini et al., 2010; Rolandone  
 185 et al., 2018). Our tests on the slip distribution robustness demonstrate that (1) Both the interevent  
 186 (Figures S7b, S10a, S10c, and S13) and the largest aftershock coseismic data (Figures S12b and  
 187 S12d) require moment release near the largest aftershock epicenter, hence, overlapping with each  
 188 other to a certain extent, (2) The overlap of the mainshock and the interevent geodetic slip is  
 189 likely due to the smoothing (Figures S10, S11c, and S12a), and (3) The largest aftershock slip

190 needs to occur at and around its epicenter (Figures S11), but the post-largest-aftershock slip there  
191 is not strongly required by the data (Figures S12b and S12d); hence the overlap of the co- and  
192 post-largest-aftershock slip is favored but not strongly supported.

193

### 194 3.2 Temporal evolution during the interevent stage

195 The inferred geodetic slip during the two interevent substages demonstrates that the slip  
196 rate decayed with time everywhere in the modeled area (Figures 2e-f, 3a, and S17), which is  
197 typical of afterslip response (e.g., Marone et al., 1991). The interevent slip is therefore essentially  
198 afterslip. It is supported also by the moving median time series illustrated as motograms (a  
199 spatial representation of the temporal evolution of horizontal motion; Figures 2a and S6),  
200 demonstrating the emergence of interevent deformation right after the mainshock occurrence and  
201 their subsequent steady decay. This means that migration of the afterslip peak is not a dominant  
202 process at the interevent stage. Yet, coastal sites near the South area show a southward deflection  
203 of the motion during the late interevent stage, starting  $\sim 15$  hours after the mainshock (Figure 2a),  
204 which is illustrated also in the displacement fields during the first and second substages (Figures  
205 2e-f). The motion of sites in the North decays more rapidly than sites in the South (Figure 2a).  
206 These features suggest a temporal change in the slip pattern and/or perhaps a feeble southward  
207 migration of aseismic slip.

208 Unlike the geodetic slip, the evolution of moderate seismicity notably indicates a  
209 significant contrast between the North and South areas (Figures 2c-d and S18). In the mainshock  
210 area (North), the moment evolution inferred from seismicity shows very rapid decay. In contrast,  
211 in the largest aftershock area (South), the geodetic slip decays over time whereas a larger seismic  
212 moment release occurred during the second substage, dominated by the M 6.1 event (Figure 2d).  
213 The acceleration of seismicity count in this area (Figure 2c) is unclear because many small  
214 events are potentially missing in the catalog (Figures S19-S20). In this area, the seismic-to-  
215 geodetic moment ratio is less than 1% during the first substage, which increased to 37.5%  
216 subsequently (Figures 2d and S14 and Table S1). Hence, the interevent slip in the South subarea  
217 became more seismic at the second substage. These features are very different from the 2015  
218 Illapel case in which both early postseismic slip and aftershocks decay with time and one  
219 postseismic slip patch is 100% seismic due to some large aftershocks (Liu et al., 2022; Twardzik  
220 et al., 2021).

221

## 222 4 Discussion and Conclusions

### 223 4.1 Along-strike megathrust heterogeneity and rupture segmentation

224 The megathrust off-Iquique, where the southernmost interevent slip peak is found, has  
225 been creeping at various earthquake cycle stages (Fig. 4a). The afterslip lasted there at least for 9  
226 months (Shrivastava et al., 2019). Various long-term interseismic locking models agree with the  
227 tendency of lower degrees of locking than the neighboring sections along-strike (Figure 4b; e.g.,  
228 Jolivet et al., 2020; Li et al., 2015; Métois et al., 2016; Schurr et al., 2014). The 8-month pre-  
229 mainshock aseismic transient (black contours in Figs. 3a-b; Socquet et al., 2017) overlaps with  
230 these aseismic slip regions. Hence, this aseismic slip area likely acted as a barrier to the

231 southward propagation of the mainshock rupture (Duputel et al., 2015; Hayes et al. 2014; Jara et  
232 al., 2018; Meng et al., 2015) (Figures 3 and 4b), and prevented the rupture of the largest  
233 aftershock and mainshock faults as a single event, despite a positive mainshock CSC at its  
234 epicenter (Fig. S9a). Our interevent aseismic slip unambiguously confirms the spatiotemporal  
235 separation of the two big quakes by this aseismic barrier, which was indirectly proposed from an  
236 analysis of the post-largest-aftershock afterslip (Shrivastava et al., 2019). Similar sequential  
237 occurrences of large earthquakes intervened by afterslip have been reported elsewhere (e.g.,  
238 Elliott et al., 2022; Klein et al., 2021; Miyazaki & Larson, 2008; Zhao et al., 2022).

239 Such creeping megathrust sections could be typically interpreted as zones of velocity-  
240 strengthening friction (Perfettini & Avouac, 2004), but this interpretation does not match with  
241 the overlap of the interevent aseismic slip, the 9-month afterslip patch (Shrivastava et al., 2019),  
242 and the largest aftershock coseismic slip. One possible interpretation would be that small  
243 seismic, velocity-weakening patches are embedded in the velocity-strengthening zone and they  
244 sometimes break altogether to form a large earthquake when they are critically loaded by  
245 surrounding creep. Locking of such small patches is not resolvable by land GNSS, so the area is  
246 imaged as an aseismic zone when the surrounding creep rate is low enough and behaves as an  
247 aseismic barrier (Figure 4; e.g., Avouac, 2015; Socquet et al., 2017). This may favor the  
248 termination of the 1877  $M_w \geq 8.5$  earthquake at off-Iquique (e.g., Vigny & Klein, 2022),  
249 although it still does not exclude the possibility of rupture through this zone (Comte & Pardo,  
250 1991; Kausel, 1986) (Figures 1a).

251 Another major controlling factor of faulting behavior is geometrical heterogeneity.  
252 Geometrical heterogeneity of faults with uniform velocity-weakening friction can realize  
253 collocation of seismic and aseismic slip (e.g., Cattania & Segall, 2021; Romanet et al. 2018).  
254 Wang and Bilek (2011) proposed that rugged faults due to seamount subduction favor slow creep  
255 more than large earthquakes. Off-Iquique, along-strike changes in gravity anomaly (Jara et al.,  
256 2018; Maksymowicz et al., 2018; Molina et al., 2021), spatial distribution of subparallel spray  
257 faults along the megathrust (Cubas et al., 2022), small seamounts on the megathrust interface  
258 (Geersen et al., 2015), local high slab topography (Storch et al., 2023) and Iquique ridge on the  
259 incoming Nazca plate have been reported (Figures 1a and S21). These observations imply that  
260 the off-Iquique megathrust has a more heterogeneous geometry and overburden stress than the  
261 neighbor segments along-strike. Such geometrical features might also be responsible for the  
262 complex mosaic of the aseismic and seismic processes there, in addition to the frictional  
263 heterogeneity.

264 The other two aseismic slip patches allow us to depict the mechanical characteristics of  
265 the megathrust north of the mainshock and the down-dip of the largest aftershock (Figure 4). To  
266 the north of the mainshock latitude, aseismic slip before and after the mainshock overlap. Excess  
267 fluid pressure along the megathrust there may prevent the accumulation of elastic strain (Ma et  
268 al., 2022). The possible termination of the 1877 rupture is located there (Figure 1a) where long-  
269 term locking rates were inferred to be low (Jolivet et al., 2020; Li et al., 2015; Métois et al. 2016;  
270 Schurr et al., 2014). We speculate that the megathrust north of the mainshock peak is a persistent  
271 aseismic barrier (Figures 3b and 4b). The interevent aseismic slip patch down-dip of the largest  
272 aftershock overlaps with the 8-month pre-mainshock slip at greater depth (Figure 4a). The  
273 locking rate is also small there (Figure 4b). This patch at great depth could be controlled by the  
274 persistent creep controlled by ductile fault rheology (e.g., Scholz, 1998). This patch is away from  
275 the mainshock peak, so the increase of aseismic slip rate following the mainshock was perhaps

276 triggered dynamically, similar to remotely triggered afterslip/slow slips by large earthquakes  
277 (e.g., Rolandone et al., 2018; Wallace et al., 2018).

278

#### 279 4.2 Evolution of seismic-aseismic interaction toward the largest aftershock

280 The revealed temporal evolution of the interevent processes hints at the preparation of the  
281 largest aftershock. The interevent aseismic slip evolved progressively in the forthcoming largest  
282 aftershock area (Figure 2a). In contrast, the seismic moment release was intermittent there  
283 (Figures 2c-d and 2g), which highlights that the interevent process does not hold a typical  
284 postseismic behavior as seen at the mainshock latitude. During the first stage, the slip is mostly  
285 aseismic (Figure S14). In the second stage, the increased seismic contribution to the total  
286 moment is dominated by the M 6.1 event 45 minutes before the largest aftershock (Figures 2c-d  
287 and 2g), which occurred only 32km away from the largest aftershock epicenter (Soto et al.,  
288 2019a). This M 6.1 event was perhaps the final kick to commence the largest aftershock rupture,  
289 although the contribution of this single event is not visible in the CSC computed from the  
290 geodetic slip (Figure S9b). Such seismic-aseismic behavior favors the rate-dependent cascade-up  
291 model for the nucleation process of the 2014 Iquique largest aftershock (Kato & Ben-Zion, 2021;  
292 McLaskey, 2019).

293 Interestingly, contrary to the larger seismic moment release during the second substage,  
294 the interevent aseismic slip quickly decayed throughout the interevent stage (Figure 2e-f; Figure  
295 S14). Numerical models and laboratory experiments usually demonstrate an acceleration of  
296 precursor aseismic slip as a part of the nucleation processes (e.g., Cattania & Segall, 2021;  
297 Dieterich, 1992; Marty et al., 2023; Noda et al., 2013). In our case, such a significant  
298 acceleration of the interevent slip was not identified. Yet, our interevent decelerating aseismic  
299 still likely acted as a stress-loading driver, destabilizing the largest aftershock fault and  
300 promoting its nucleation. This loading perhaps started with the 8-month pre-mainshock slow slip  
301 (Figure 4; Socquet et al., 2017) and the increased aseismic slip rate triggered by the mainshock  
302 played a role in critically destabilizing the largest aftershock fault. In this regard, the negative  
303 CSC due to the interevent slip in the largest aftershock epicentral area probably reflects a  
304 cumulative stress drop associated with the nucleation including the contribution from the M 6.1  
305 (Figure S9b). The absolute interevent CSC value highly depends on the slip smoothing, so only  
306 the sign is considered meaningful here.

307 Another intriguing question relates to the delayed occurrence of the largest aftershock.  
308 Our analysis does not quantitatively explain the timing of this delay. Such delay is sometimes  
309 controlled by migrating slow slip (Ariyoshi et al., 2019; Cebry et al., 2022), but our seismic and  
310 aseismic observations do not support it as the dominant process (Figures 2a and 2e-g).  
311 Determination of the timing of large aftershocks is still an unresolved issue even after revealing  
312 the nucleation mechanism.

313

#### 314 **Acknowledgments**

315 The authors declare no conflicts of interest. We appreciate thoughtful reviews from the  
316 Editor Germán Prieto, Roland Burgmann and four anonymous reviewers to this or an earlier

317 version manuscript, which highly improved this study. Discussion with Jorge Jara, Zaccaria El  
318 Yousfi, Ian McBrearty, Taku Ueda, Michel Bouchon, Satoshi Ide, Jean-Philippe Avouac, and  
319 Sylvain Barbot was fruitful. Nadaya Cubas and Hui Huang provided us with the results of Cubas  
320 et al. (2022) and Meng et al. (2015), respectively. Aubin Tsapong helped check the quality of  
321 raw GPS observations. Geoffrey Blewitt answered our questions on their data processing  
322 strategy at NGL. We used Generic Mapping Tools (Wessel et al., 2013) to draw the figures.  
323 English check of an earlier version manuscript by James Hollingsworth helped improve the  
324 manuscript. Y.I. is a Japan Society for the Promotion of Science (JSPS) Overseas Research  
325 Fellow. This study is supported by Japan Society for the Promotion of Science (JSPS) Overseas  
326 Research Fellowships and KAKENHI 21K14007 and 21K03694 (YI) and ERC CoG 865963  
327 DEEP-trigger (AS).

328

### 329 **Open Research**

330 We processed only published results/data and no new data were acquired. The GPS coordinates  
331 (Blewitt et al., 2018) are available from Nevada Geodetic Laboratory (2022). The seismicity  
332 catalog of Soto et al. (2019a) is available from Soto et al. (2019b). The gravity anomaly  
333 (Sandwell et al., 2014) and topography (Smith & Sandwell, 1997) data are available from  
334 Scripps Institution of Oceanography (2022). The inversion code SDM (Wang et al., 2009, 2013a)  
335 is available from Wang et al. (2013b). We used a Fortran 90 translation of the DC3D subroutine  
336 (Okada, 1992) provided by Miyashita (2020). We made our processed GPS displacements and  
337 slip distributions available in Zenodo as Itoh et al. (2023).

338

### 339 **References**

- 340 Ariyoshi, K., Ampuero, J. P., Bürgmann, R., Matsuzawa, T., Hasegawa, A., Hino, R., & Hori, T.  
341 (2019). Quantitative relationship between aseismic slip propagation speed and frictional  
342 properties. *Tectonophysics*, 767, 128151. <https://doi.org/10.1016/j.tecto.2019.06.021>
- 343 Avouac, J. P. (2015). From geodetic imaging of seismic and aseismic fault slip to dynamic  
344 modeling of the seismic cycle. *Annual Review of Earth and Planetary Sciences*, 43, 233-271.  
345 <https://doi.org/10.1146/annurev-earth-060614-105302>
- 346 Bedford, J., Moreno, M., Schurr, B., Bartsch, M., & Oncken, O. (2015), Investigating the final  
347 seismic swarm before the Iquique-Pisagua 2014 Mw 8.1 by comparison of continuous GPS and  
348 seismic foreshock data. *Geophysical Research Letters*, 42, 3820–3828.  
349 <https://doi.org/10.1002/2015GL063953>
- 350 Blewitt, G., Hammond, W. C., & Kreemer, C. (2018). Harnessing the GPS data explosion for  
351 interdisciplinary science. *Eos*, 99. <https://doi.org/10.1029/2018EO104623>
- 352 Bock, Y., Nikolaidis, R. M., de Jonge, P. J., & Bevis, M. (2000). Instantaneous geodetic  
353 positioning at medium distances with the Global Positioning System. *Journal of Geophysical*  
354 *Research: Solid Earth* 105, 28223–28253. <https://doi.org/10.1029/2000JB900268>
- 355 Boudin, F., et al. (2022). Slow slip events precursory to the 2014 Iquique Earthquake, revisited  
356 with long-base tilt and GPS records, *Geophysical Journal International* 228, 2092–2121.  
357 <https://doi.org/10.1093/gji/ggab425>

- 358 Caballero, E., Chounet, A., Duputel, Z., Jara, J., Twardzik, C., & Jolivet, R. (2021). Seismic and  
359 aseismic fault slip during the initiation phase of the 2017  $M_W = 6.9$  Valparaíso earthquake.  
360 *Geophysical Research Letters*, 48, e2020GL091916. <https://doi.org/10.1029/2020GL091916>
- 361 Cattania, C., & Segall, P. (2021). Precursory slow slip and foreshocks on rough faults. *Journal of*  
362 *Geophysical Research: Solid Earth* 126, e2020JB020430. <https://doi.org/10.1029/2020JB020430>
- 363 Cebry, S. B. L., Ke, C. Y., Shreedharan, S. Marone, C., Kammer, D. S., McLaskey, G. C. (2022).  
364 Creep fronts and complexity in laboratory earthquake sequences illuminate delayed earthquake  
365 triggering. *Nature Communications*, 13, 6839. <https://doi.org/10.1038/s41467-022-34397-0>
- 366 Cleveland, R. B., Cleveland, W. S., McRae, J. E., & Terpenning, I. (1990). STL: A seasonal-  
367 trend decomposition procedure based on loess. *Journal of Official Statistics*, 6, 3–73
- 368 Comte, D., & Pardo, M. (1991). Reappraisal of great historical earthquakes in the northern Chile  
369 and southern Peru seismic gaps. *Natural Hazards*, 4, 23–44. <https://doi.org/10.1007/BF00126557>
- 370 Cubas, N., Agard, P., & Tissandier, R. (2022). Earthquake ruptures and topography of the  
371 Chilean margin controlled by plate interface deformation. *Solid Earth* 13, 779–792.  
372 <https://doi.org/10.5194/se-13-779-2022>
- 373 DeMets, C., Gordon, R. G., & Argus, D. F. (2010). Geologically current plate motions.  
374 *Geophysical Journal International*, 181, 1–80. <https://doi.org/10.1111/j.1365-246X.2009.04491.x>
- 376 Dieterich, J. H. (1992). Earthquake nucleation on faults with rate-and state-dependent strength.  
377 *Tectonophysics*, 211, 115-134. [https://doi.org/10.1016/0040-1951\(92\)90055-B](https://doi.org/10.1016/0040-1951(92)90055-B)
- 378 Duputel, Z., et al. (2015). The Iquique earthquake sequence of April 2014: Bayesian modeling  
379 accounting for prediction uncertainty, *Geophysical Research Letters*, 42, 7949–7957.  
380 <https://doi.org/10.1002/2015GL065402>
- 381 Elliott, J. L., Grapenthin, R., Parameswaran, R. M., Xiao, Z., Freymueller, J. T., & Fusso, L.  
382 (2022). Cascading rupture of a megathrust. *Science Advances*, 8, eabm4131.  
383 <https://doi.org/10.1126/sciadv.abm4131>
- 384 Geersen, J., Ranero, C., Barckhausen, U., & Reichert, C. (2015), Subducting seamounts control  
385 interplate coupling and seismic rupture in the 2014 Iquique earthquake area. *Nature*  
386 *Communications*, 6, 8267. <https://doi.org/10.1038/ncomms9267>
- 387 Herman, M. W., Furlong, K. P., Hayes, G. P., & Benz, H. M. (2016). Foreshock triggering of the  
388 1 April 2014  $M_w$  8.2 Iquique, Chile, earthquake. *Earth and Planetary Science Letters*, 447, 119-  
389 129. <https://doi.org/10.1016/j.epsl.2016.04.020>
- 390 Hayes, G. (2018). Slab2 - A comprehensive subduction zone geometry model. *U.S. Geological*  
391 *Survey data release*.
- 392 Hayes, G., et al. (2014). Continuing megathrust earthquake potential in Chile after the 2014  
393 Iquique earthquake. *Nature*, 512, 295–298. <https://doi.org/10.1038/nature13677>
- 394 Hoffmann, F., Metzger, S., Moreno, M., Deng, Z., Sippl, C., Ortega-Culaciati, F., & Oncken, O.  
395 (2018). Characterizing afterslip and ground displacement rate increase following the 2014  
396 Iquique-Pisagua  $M_w$  8.1 earthquake, Northern Chile. *Journal of Geophysical Research: Solid*  
397 *Earth*, 123, 4171–4192. <https://doi.org/10.1002/2017JB014970>

- 398 Ito, Y., et al. (2013). Episodic slow slip events in the Japan subduction zone before the 2011  
399 Tohoku-Oki earthquake. *Tectonophysics*, 600, 14-26. <https://doi.org/10.1016/j.tecto.2012.08.022>
- 400 Itoh, Y., & Aoki, Y. (2022). On the performance of position-domain sidereal filter for 30-s  
401 kinematic GPS to mitigate multipath errors. *Earth, Planets and Space*, 74, 23.  
402 <https://doi.org/10.1186/s40623-022-01584-8>
- 403 Itoh, Y., Nishimura, T., Ariyoshi, K., & Matsumoto, H. (2019). Interplate slip following the 2003  
404 Tokachi-oki earthquake from ocean bottom pressure gauge and land GNSS data. *Journal of*  
405 *Geophysical Research: Solid Earth*, 124, 4205–4230. <https://doi.org/10.1029/2018JB016328>
- 406 Itoh, Y., Socquet, A., & Radiguet, M. (2023). Dataset for the paper "Largest aftershock  
407 nucleation driven by afterslip during the 2014 Iquique sequence" (Version 1) [Data set]. Zenodo.  
408 <https://doi.org/10.5281/zenodo.10201545>
- 409 Jara, J., et al. (2018). Kinematic study of Iquique 2014 Mw 8.1 earthquake: Understanding the  
410 segmentation of the seismogenic zone. *Earth and Planetary Science Letters*, 503, 131-143.  
411 <https://doi.org/10.1016/j.epsl.2018.09.025>
- 412 Jiang, J., Klein, E., & Bock, Y. (2021). Coevolving early afterslip and aftershock signatures of a  
413 San Andreas fault rupture. *Science Advances*, 7, eabc1606  
414 <https://doi.org/10.1126/sciadv.abc1606>
- 415 Jolivet, R., Simons, M., Duputel, Z., Olive, J.-A., Bhat, H. S., & Bletery, Q. (2020). Interseismic  
416 loading of subduction megathrust drives long-term uplift in Northern Chile. *Geophysical*  
417 *Research Letters*, 47, e2019GL085377. <https://doi.org/10.1029/2019GL085377>
- 418 Kaneko, Y., Avouac, J.-P. & Lapusta, N. (2010). Towards inferring earthquake patterns from  
419 geodetic observations of interseismic coupling. *Nature Geosciences*, 3, 363–369.  
420 <https://doi.org/10.1038/ngeo843>
- 421 Kato, A., & Ben-Zion, Y. (2021). The generation of large earthquakes. *Nature Reviews Earth &*  
422 *Environment* 2, 26–39. <https://doi.org/10.1038/s43017-020-00108-w>
- 423 Kausel, E. (1986). Los terremotos de agosto de 1868 y mayo de 1877 que afectaron el sur del  
424 Perú y norte de Chile. *Boletín de la Academia Chilena de Ciencias* 3, 8–13
- 425 Kato, A., Fukuda, J., Kumazawa, T., & Nakagawa, S. (2016). Accelerated nucleation of the 2014  
426 Iquique, Chile Mw 8.2 Earthquake. *Scientific Reports*, 6, 24792  
427 <https://doi.org/10.1038/srep24792>
- 428 Kato, A., Obara, K., Igarashi, T., Tsuruoka, H., Nakagawa, S., & Hirata, N. (2012) Propagation  
429 of Slow Slip Leading Up to the 2011 Mw 9.0 Tohoku-Oki Earthquake. *Science* 335, 705-708.  
430 <https://doi.org/10.1126/science.1215141>
- 431 King, G. C. P., Stein, S. S., Lin, J. (1994). Static stress changes and the triggering of earthquakes.  
432 *Bulletin of Seismological Society of America*. 84, 935–953.  
433 <https://doi.org/10.1785/BSSA0840030935>
- 434 Klein, E. (2021). Interplay of seismic and a-seismic deformation during the 2020 sequence of  
435 Atacama, Chile. *Earth and Planetary Science Letters* 570, 117081.  
436 <https://doi.org/10.1016/j.epsl.2021.117081>

- 437 Li, S., Moreno, M., Bedford, J., Rosenau, M., Oncken, O. (2015). Revisiting viscoelastic effects  
438 on interseismic deformation and locking degree: A case study of the Peru-North Chile  
439 subduction zone. *Journal of Geophysical Research: Solid Earth* 120, 4522–4538.  
440 <https://doi.org/10.1002/2015JB011903>
- 441 Liu, K., Geng, J., Wen, Y., Ortega-Culaciati, F., & Comte, D. (2022). Very early postseismic  
442 deformation following the 2015 Mw 8.3 Illapel earthquake, Chile revealed from kinematic GPS.  
443 *Geophysical Research Letters*, 49, e2022GL098526. <https://doi.org/10.1029/2022GL098526>
- 444 Ma, B., et al., (2022). Megathrust reflectivity reveals the updip limit of the 2014 Iquique  
445 earthquake rupture. *Nature Communications* 13, 3969. [https://doi.org/10.1038/s41467-022-](https://doi.org/10.1038/s41467-022-31448-4)  
446 [31448-4](https://doi.org/10.1038/s41467-022-31448-4)
- 447 Maksymowicz, A., Ruiz, J., Vera, E., Contreras-Reyes, E., Ruiz, S., Arraigada, C., Bonvalot, S.,  
448 & Bascuñan, S. (2018). Heterogeneous structure of the Northern Chile marine forearc and its  
449 implications for megathrust earthquakes. *Geophysical Journal International* 215, 1080–1097.  
450 <https://doi.org/10.1093/gji/ggy325>
- 451 Marill, L., Marsan, D., Socquet, A., Radiguet, M., Cotte, N., & Rousset, B., (2021). Fourteen-  
452 year acceleration along the Japan Trench. *Journal of Geophysical Research: Solid Earth* 126,  
453 e2020JB021226. <https://doi.org/10.1029/2020JB021226>
- 454 Marone, C. J., Scholz, C. H., & Bilham, R. (1991). On the mechanics of earthquake afterslip,  
455 *Journal of Geophysical Research: Solid Earth* 96, 8441–8452.  
456 <https://doi.org/10.1029/91JB00275>
- 457 Marty, S., Schubnel, A., Bhat, H. S., Aubry, J., Fukuyama, E., Latour, S., et al. (2023).  
458 Nucleation of laboratory earthquakes: Quantitative analysis and scalings. *Journal of Geophysical*  
459 *Research: Solid Earth*, 128, e2022JB026294. <https://doi.org/10.1029/2022JB026294>
- 460 Mavrommatis, A. P., Segall, P., & Johnson, K. M. (2014). A decadal-scale deformation transient  
461 prior to the 2011  $M_w$  9.0 Tohoku-oki earthquake, *Geophysical Research Letters*, 41, 4486–4494.  
462 <https://doi.org/10.1002/2014GL060139>
- 463 McBrearty, I. W., Gomberg, J., Delorey, A. A., & Johnson, P. A. (2019). Earthquake Arrival  
464 Association with Backprojection and Graph Theory. *Bulletin of Seismological Society of*  
465 *America* 109, 2510–2531. <https://doi.org/10.1785/0120190081>
- 466 McLaskey, G. C. (2019). Earthquake Initiation From Laboratory Observations and Implications  
467 for Foreshocks. *Journal of Geophysical Research: Solid Earth*, 124, 12882–12904.  
468 <https://doi.org/10.1029/2019JB018363>
- 469 Meng, L., Huang, H., Bürgmann, R., Ampuero, J.-P., & Strader, A. (2015). Dual megathrust slip  
470 behaviors of the 2014 Iquique earthquake sequence. *Earth and Planetary Science Letters* 411,  
471 177-187. <https://doi.org/10.1016/j.epsl.2014.11.041>
- 472 Métois, M., Vigny, C., & Socquet, A. (2016). Interseismic Coupling, Megathrust Earthquakes  
473 and Seismic Swarms Along the Chilean Subduction Zone (38°–18°S). *Pure and Applied*  
474 *Geophysics* 173, 1431–1449. <https://doi.org/10.1007/s00024-016-1280-5>
- 475 Miyashita, T. (2020). DC3D.f90: January 14, 2020 Release [Software] Github  
476 <https://github.com/hydrocoast/DC3D.f90>

- 477 Miyazaki, S., & Larson, K. M. (2008). Coseismic and early postseismic slip for the 2003  
478 Tokachi-oki earthquake sequence inferred from GPS data. *Geophysical Research Letters* 35,  
479 L04302. <https://doi.org/10.1029/2007GL032309>
- 480 Miyazaki, S., Segall, P., Fukuda, J., & Kato, T. (2004). Space time distribution of afterslip  
481 following the 2003 Tokachi-oki earthquake: Implications for variations in fault zone frictional  
482 properties. *Geophysical Research Letters*, 31, L06623, <https://doi.org/10.1029/2003GL019410>
- 483 Molina, D., Tassara, A., Abarca, R., Melnick, D., & Madella, A. (2021). Frictional segmentation  
484 of the Chilean megathrust from a multivariate analysis of geophysical, geological, and geodetic  
485 data. *Journal of Geophysical Research: Solid Earth*, 126, e2020JB020647  
486 <https://doi.org/10.1029/2020JB020647>
- 487 Nevada Geodetic Laboratory (2022). [Dataset] <http://geodesy.unr.edu/>
- 488 Nishikawa, T., Matsuzawa, T., Ohta, K., Nishimura, T. & Ide, S. (2019). The slow earthquake  
489 spectrum in the Japan Trench illuminated by the S-net seafloor observatories. *Science* 365, 808-  
490 813. <https://doi.org/10.1126/science.aax5618>
- 491 Noda, H., Nakatani, M., & Hori, T. (2013), Large nucleation before large earthquakes is  
492 sometimes skipped due to cascade-up—Implications from a rate and state simulation of faults  
493 with hierarchical asperities, *Journal of Geophysical Research: Solid Earth*, 118, 2924– 2952.  
494 <https://doi.org/10.1002/jgrb.50211>
- 495 Ohta, Y., et al. (2012). Geodetic constraints on afterslip characteristics following the March 9,  
496 2011, Sanriku-oki earthquake, Japan. *Geophysical Research Letters*, 39, L16304,  
497 <https://doi.org/10.1029/2012GL052430>
- 498 Okada, Y. (1992). Internal deformation due to shear and tensile faults in a half-space. *Bulletin of*  
499 *Seismological Society of America*, 82, 1018–1040. <https://doi.org/10.1785/BSSA0820021018>
- 500 Perfettini, H., & Avouac, J. P. (2004). Postseismic relaxation driven by brittle creep: A possible  
501 mechanism to reconcile geodetic measurements and the decay rate of aftershocks, application to  
502 the Chi-Chi earthquake, Taiwan. *Journal of Geophysical Research: Solid Earth*, 109, B02304.  
503 <https://doi.org/10.1029/2003JB002488>
- 504 Perfettini, H., et al. (2010). Seismic and aseismic slip on the Central Peru megathrust. *Nature*  
505 465, 78–81. <https://doi.org/10.1038/nature09062>
- 506 Perfettini, H., Frank, W. B., Marsan, D., & Bouchon, M. (2018). A model of aftershock migration  
507 driven by afterslip. *Geophysical Research Letters*, 45, 2283– 2293.  
508 <https://doi.org/10.1002/2017GL076287>
- 509 Periollat, A., Radiguet, M., Weiss, J., Twardzik, C., Amitrano, D., Cotte, N., Marill, L., &  
510 Socquet, A. (2022). Transient brittle creep mechanism explains early postseismic phase of the  
511 2011 Tohoku-Oki megathrust earthquake: Observations by high-rate GPS solutions. *Journal of*  
512 *Geophysical Research: Solid Earth*, 127, e2022JB024005.  
513 <https://doi.org/10.1029/2022JB024005>
- 514 Ragheb, A. E., Clarke, P. J., & Edwards, S. J. (2007). GPS sidereal filtering: Coordinate- and  
515 carrier-phase-level strategies. *Journal of Geodesy*, 81, 325–335. [https://doi.org/10.1007/s00190-  
516 006-0113-1](https://doi.org/10.1007/s00190-006-0113-1)

- 517 Rolandone, F., et al., (2018). Areas prone to slow slip events impede earthquake rupture  
518 propagation and promote afterslip. *Science Advances*, 4, eaao6596.  
519 <https://doi.org/10.1126/sciadv.aao6596>
- 520 Romanet, P., Bhat, H. S., Jolivet, R., & Madariaga, R. (2018). Fast and slow slip events emerge  
521 due to fault geometrical complexity. *Geophysical Research Letters*, 45, 4809–4819.  
522 <https://doi.org/10.1029/2018GL077579>
- 523 Ruiz, S., Metois, M., Fuenzalida, A., Ruiz, J., Leyton, F., Grandin, R., Vigny, C., Madariaga, R.,  
524 & Campos, J. (2014). Intense foreshocks and a slow slip event preceded the 2014 Iquique Mw  
525 8.1 earthquake. *Science*, 345, 1165-1169. <https://doi.org/10.1126/science.1256074>
- 526 Sandwell, D. T., Müller, R. D., Smith, W. H. F., Garcia, E., & Francis, R. (2014). New global  
527 marine gravity model from CryoSat-2 and Jason-1 reveals buried tectonic structure. *Science*,  
528 346, 65-67. <https://doi.org/10.1126/science.1258213>
- 529 Scholz, C. (1998). Earthquakes and friction laws. *Nature*, 391, 37–42  
530 <https://doi.org/10.1038/34097>
- 531 Scripps Institution of Oceanography (2022). EXTRACT XYZ GRID - TOPOGRAPHY OR  
532 GRAVITY. V19.1 and V29.1 for topography and gravity, respectively [Dataset]  
533 [https://topex.ucsd.edu/cgi-bin/get\\_data.cgi](https://topex.ucsd.edu/cgi-bin/get_data.cgi)
- 534 Schurr, B., et al. (2014). Gradual unlocking of plate boundary controlled initiation of the 2014  
535 Iquique earthquake. *Nature*, 512, 299–302. <https://doi.org/10.1038/nature13681>
- 536 Shrivastava, M. N., González, G., Moreno, M., Soto, H., Schurr, B., Salazar, P., Báez, J. C.  
537 (2019). Earthquake segmentation in northern Chile correlates with curved plate geometry.  
538 *Scientific Reports*, 9, 4403. <https://doi.org/10.1038/s41598-019-40282-6>
- 539 Sippl, C., Schurr, B., Asch, G., & Kummerow, J. (2018). Seismicity structure of the northern  
540 Chile forearc from >100,000 double-difference relocated hypocenters. *Journal of Geophysical*  
541 *Research: Solid Earth*, 123, 4063–4087. <https://doi.org/10.1002/2017JB015384>
- 542 Smith, W. H. F., & Sandwell, D. T. (1997). Global seafloor topography from satellite altimetry  
543 and ship depth soundings. *Science* 277, 1957-1962.  
544 <https://doi.org/10.1126/science.277.5334.1956>
- 545 Socquet, A., et al. (2017). An 8 month slow slip event triggers progressive nucleation of the 2014  
546 Chile megathrust, *Geophysical Research Letters*, 44, 4046–4053.  
547 <https://doi.org/10.1002/2017GL073023>
- 548 Soto, H., Sippl, C., Schurr, B., Kummerow, J., Asch, G., Tilmann, F., Comte, D., Ruiz, S., &  
549 Oncken, O. (2019a). Probing the northern Chile megathrust with seismicity: the 2014 M8.1  
550 iquique earthquake sequence. *Journal of Geophysical Research: Solid Earth*, 124, 12935–12954.  
551 <https://doi.org/10.1029/2019JB017794>
- 552 Soto, H., Sippl, C., Schurr, B., Kummerow, J., Asch, G., Tilmann, F., Comte, D., Ruiz, S., &  
553 Oncken, O. (2019b). Catalogue of Hypocenters for the 2014 M8.1 Iquique Earthquake Sequence,  
554 recorded by IPOC (plus additional) seismic stations. [Dataset] *GFZ Data Services*.  
555 <https://doi.org/10.5880/GFZ.4.1.2019.009>

- 556 Storch, I., Buske, S., Victor, P., & Oncken, O. (2023). A topographic depression on the  
557 subducting Nazca plate controls the April 1st 2014 M8.1 Iquique earthquake rupture in Northern  
558 Chile. *Tectonophysics*, 847, 229684. <https://doi.org/10.1016/j.tecto.2022.229684>
- 559 Tsang, L. L. H., et al. (2019). Imaging rapid early afterslip of the 2016 Pedernales earthquake,  
560 Ecuador. *Earth and Planetary Science Letters*, 524, 115724.  
561 <https://doi.org/10.1016/j.epsl.2019.115724>
- 562 Twardzik, C., Duputel, Z., Jolivet, R., Klein, E., & Reischung, P. (2022). Bayesian inference on  
563 the initiation phase of the 2014 Iquique, Chile, earthquake. *Earth and Planetary Science Letters*,  
564 600, 117835. <https://doi.org/10.1016/j.epsl.2022.117835>
- 565 Twardzik, C., Vergnolle, M., Sladen, A., & Tsang, L. L. H. (2021). Very early identification of a  
566 bimodal frictional behavior during the post-seismic phase of the 2015 Mw 8.3 Illapel, Chile,  
567 earthquake. *Solid Earth*, 12, 2523–2537. <https://doi.org/10.5194/se-12-2523-2021>
- 568 Vigny, C., & Klein, E. (2022). The 1877 megathrust earthquake of North Chile two times  
569 smaller than thought? A review of ancient articles. *Journal of South American Earth Sciences*,  
570 117, 103878. <https://doi.org/10.1016/j.jsames.2022.103878>
- 571 Wallace, L. M., Hreinsdóttir, S., Ellis, S., Hamling, I., D'Anastasio, E., & Denys, P. (2018).  
572 Triggered slow slip and afterslip on the southern Hikurangi subduction zone following the  
573 Kaikōura earthquake. *Geophysical Research Letters*, 45, 4710–4718.  
574 <https://doi.org/10.1002/2018GL077385>
- 575 Wang, K., & Bilek, S. L. (2011). Do subducting seamounts generate or stop large earthquakes?  
576 *Geology*, 39, 819–822. <https://doi.org/10.1130/G31856.1>
- 577 Wang, L., Wang, R., Roth, F., Enescu, B., Hainzl, S., & Ergintav, S. (2009). Afterslip and  
578 viscoelastic relaxation following the 1999 M 7.4 Izmit earthquake from GPS measurements,  
579 *Geophysical Journal International*, 178, 1220–1237. [https://doi.org/10.1111/j.1365-  
580 246X.2009.04228.x](https://doi.org/10.1111/j.1365-246X.2009.04228.x)
- 581 Wang, R., Diao, F., Hoechner, A. (2013a). *SDM – A geodetic inversion code incorporating with  
582 layered crust structure and curved fault geometry* Paper presented at General Assembly  
583 European Geosciences Union, Vienna, Austria. [https://gfzpublic.gfz-  
584 potsdam.de/pubman/faces/ViewItemOverviewPage.jsp?itemId=item\\_1975902](https://gfzpublic.gfz-potsdam.de/pubman/faces/ViewItemOverviewPage.jsp?itemId=item_1975902)
- 585 Wang, R., Diao, F., Hoechner, A. (2013b). *SDM – A geodetic inversion code incorporating with  
586 layered crust structure and curved fault geometry: [Software]* [ftp://ftp.gfz-  
587 potsdam.de/pub/home/turk/wang/](ftp://ftp.gfz-potsdam.de/pub/home/turk/wang/)
- 588 Wdowinski, S., Bock, Y., Zhang, J., Fang, P., & Genrich, J. (1997). Southern California  
589 permanent GPS geodetic array: Spatial filtering of daily positions for estimating coseismic and  
590 postseismic displacements induced by the 1992 Landers earthquake. *Journal of Geophysical  
591 Research: Solid Earth*, 102, 18057–18070. <https://doi.org/10.1029/97JB01378>
- 592 Wessel, P., Smith W. H. F., Scharroo, R., Luis, J., & Wobbe F. (2013). Generic Mapping Tools:  
593 Improved Version Released. *EOS*, 94, 409–410. <https://doi.org/10.1002/2013EO450001>.
- 594 Yokota, Y., & Koketsu, K. (2015). A very long-term transient event preceding the 2011 Tohoku  
595 earthquake. *Nature Communications*, 6, 5934. <https://doi.org/10.1038/ncomms6934>

596 Zhao, B., Bürgmann, R., Wang, D., Zhang, J., Yu, J., & Li, Q. (2022). Aseismic slip and recent  
597 ruptures of persistent asperities along the Alaska-Aleutian subduction zone. *Nature*  
598 *Communications*, 13, 3098. <https://doi.org/10.1038/s41467-022-30883-7>

599

600 **References only in supporting information**

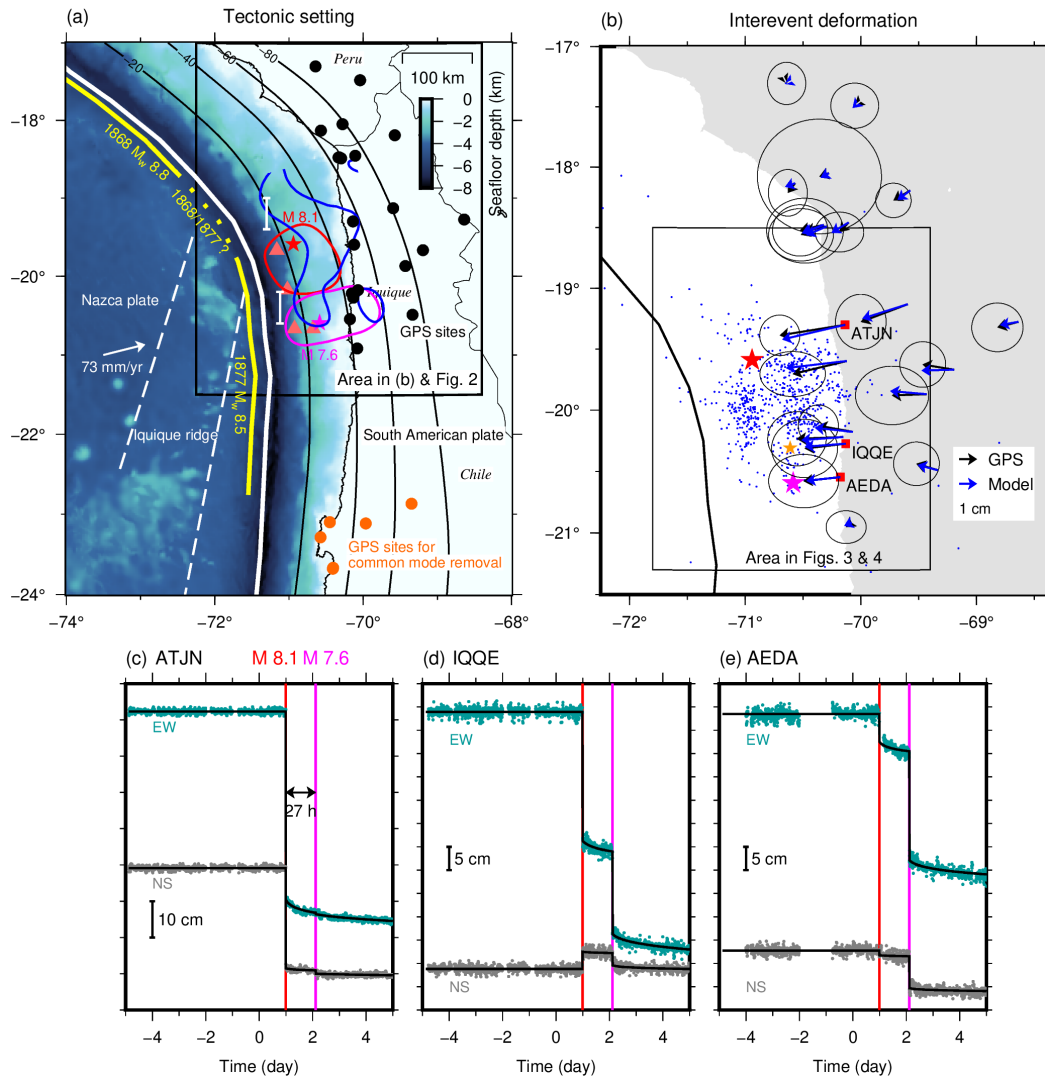
601 Altamimi, Z., Métivier, L., Rebischung, P., Rouby, H., & Collilieux, X. (2017). ITRF2014 plate  
602 motion model. *Geophysical Journal International* 209, 1906–1912.  
603 <https://doi.org/10.1093/gji/ggx136>

604 Itoh, Y., Aoki, Y., & Fukuda, J. (2022). Imaging evolution of Cascadia slow-slip event using  
605 high-rate GPS. *Scientific Reports*, 12, 7179. <https://doi.org/10.1038/s41598-022-10957-8>

606 Moutote, L., Itoh, Y., Lengliné, O., Duputel, Z., & Socquet, A. (2023). Evidence of a transient  
607 aseismic slip driving the 2017 Valparaiso earthquake sequence, from foreshocks to aftershocks.  
608 *Journal of Geophysical Research: Solid Earth*, 128, e2023JB026603.  
609 <https://doi.org/10.1029/2023JB026603>

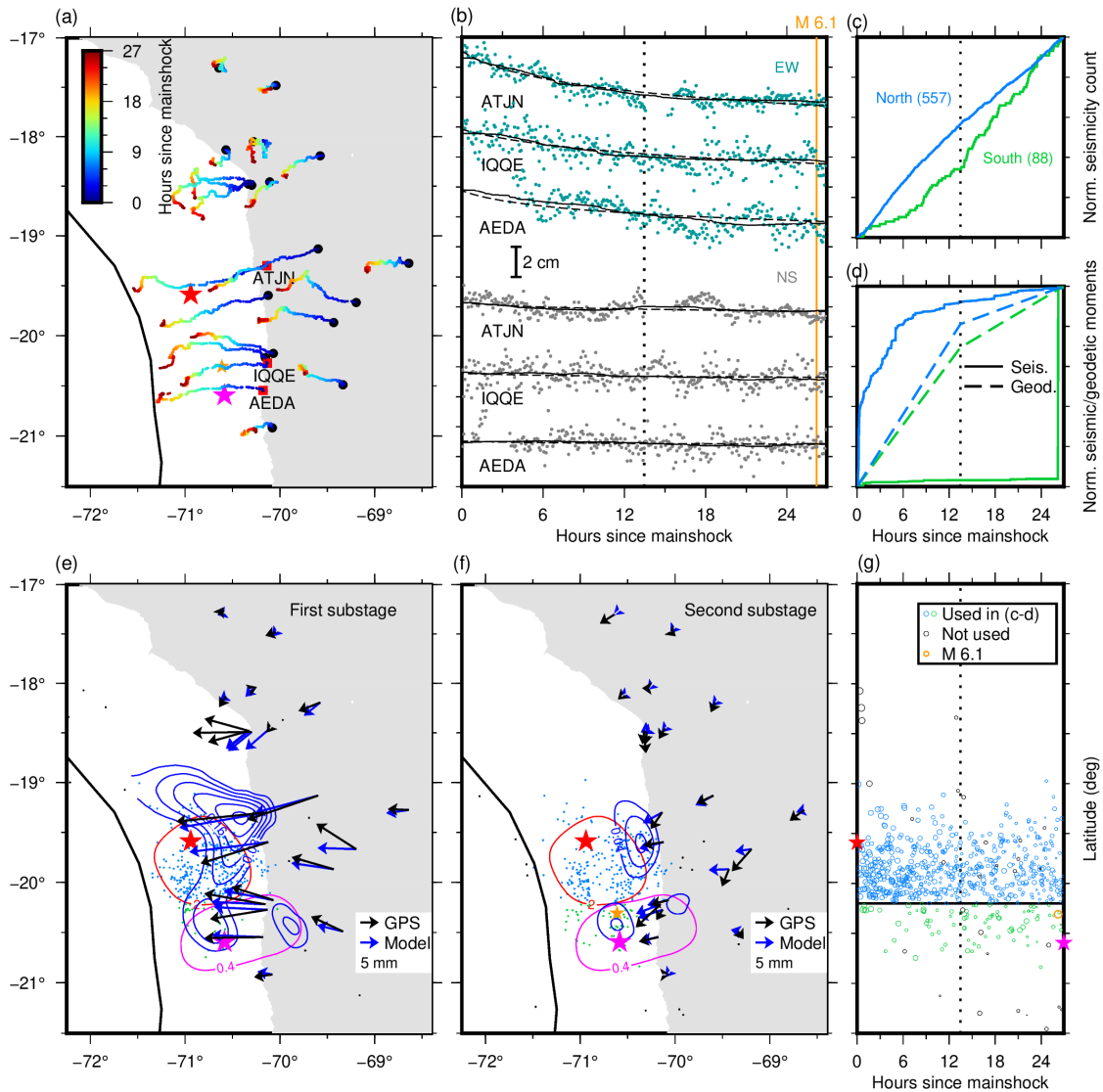
610 Pedregosa, F., et al. (2011). Scikit-learn: Machine learning in Python. *Journal of Machine*  
611 *Learning Research* 12, 2825–2830.

612



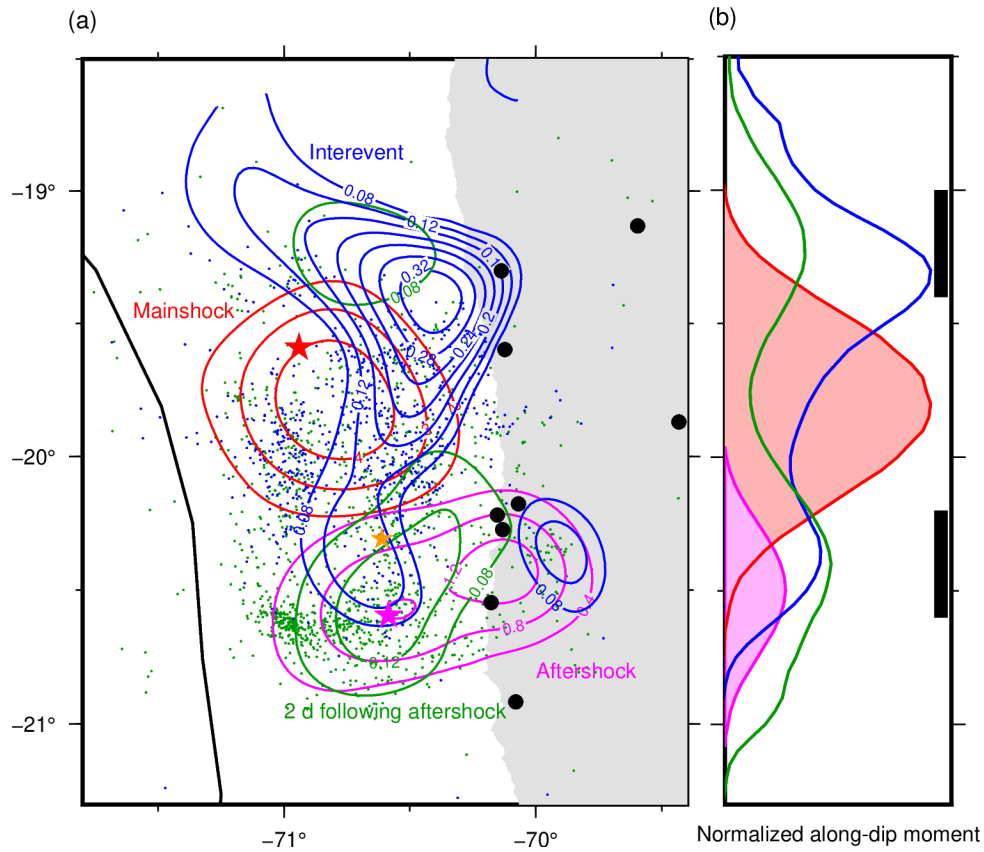
613

614 **Figure 1.** (a) Tectonic setting. Black and orange dots indicate GPS sites for deformation analysis  
 615 and common mode noise extraction, respectively. Red and magenta stars indicate the epicenters  
 616 of the 2014 Iquique mainshock and the largest aftershock, respectively (Soto et al., 2019a). Red,  
 617 blue, and magenta curves outline slip areas of the mainshock, interevent afterslip, and the largest  
 618 aftershock, respectively. A white arrow indicates the plate convergence motion (DeMets et al.,  
 619 2010). Solid contours indicate slab depth (Hayes, 2018). Yellow curves indicate rupture  
 620 extension of large earthquakes with an uncertain section dotted (Comte & Pardo, 1991; Kausel,  
 621 1986). Triangles indicate seismically imaged seamounts at the interface (Geersen et al., 2015).  
 622 White bars offshore indicate the extent of inferred aseismic barriers. (b) Interevent horizontal  
 623 GPS displacements with model prediction from slip inversion (Figure 3a). Blue dots indicate  
 624 interevent seismicity (McBrearty et al., 2019). The orange star indicates the M 6.1 epicenter  
 625 (Soto et al., 2019a). (c-e) Cleaned 5-minute GPS coordinates at labeled sites (location in (b))  
 626 with trajectory model fits (black curves).



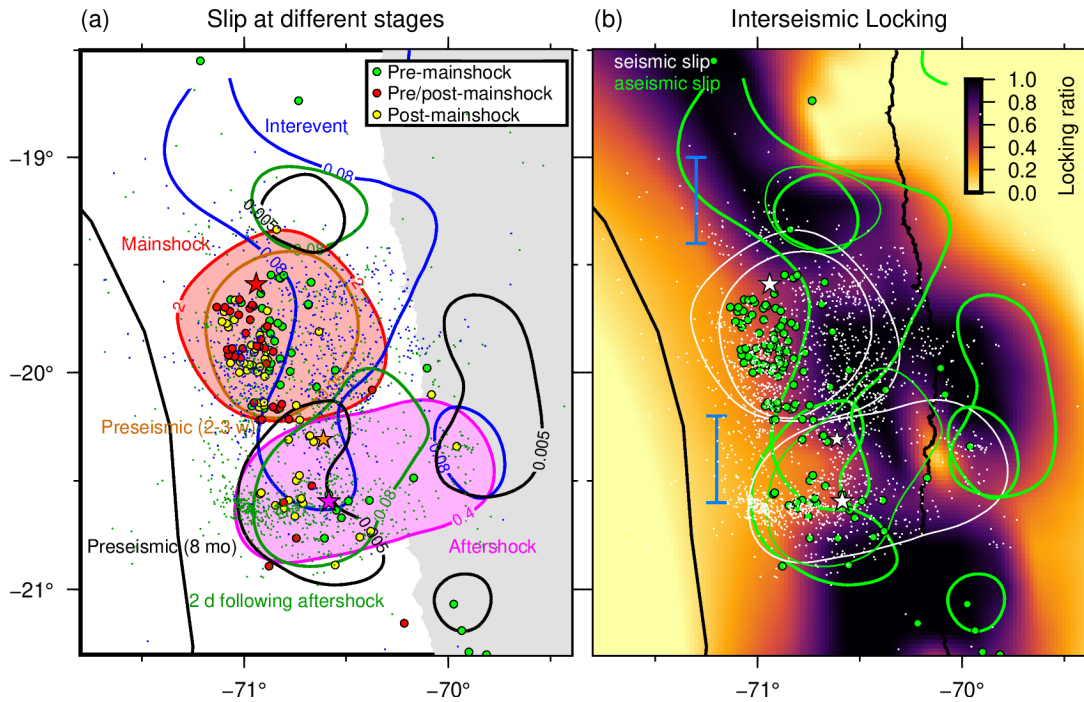
627

628 **Figure 2.** (a) Interevent GPS site motion drawn as motogram. (b) Interevent GPS coordinates  
 629 (dots; location in (a)) and their moving median (0.5-day window; solid lines) and trajectory  
 630 model fit (Figures 1c-e; broken lines). A dotted vertical line shows the middle point of the  
 631 interevent stage. (c) Normalized seismicity count (the total number in parentheses) in the two  
 632 regions divided at 20.2°S as labeled. Events accounted for in the calculation (McBrearty et al.,  
 633 2019) are shown in (e-f) with corresponding colors. (d) Same as (c) but with normalized seismic  
 634 and geodetic moment as labeled (the values presented in Table S1). (e-f) Interevent afterslip  
 635 snapshots (contour labels in m) by inverting incremental displacements (black vectors; see (b)).  
 636 Displacement error ellipses are trimmed for clarity. Displacements at sites north of 19°S are not  
 637 inverted. See Figures 1 and 3 for other elements. (g) Interevent seismicity (open circles scaled  
 638 with magnitude).



639

640 **Figure 3.** (a) Comparison of the slip at the four stages as labeled, inferred from displacements  
 641 with the trajectory model fit (Figures 1b-e, S2a-c, and S10a-f). Blue and green dots are moderate  
 642 seismicity during the corresponding stages in color (McBrearty et al., 2019). See Figure 1 for  
 643 other elements. (b) Normalized along-dip moment of each stage (colors in (a)). Coseismic (red  
 644 and magenta) and substantially aseismic (blue and green) moments are separately normalized  
 645 with respect to their maximum values (ratio of the two normalizing factors is  $\sim 0.056$ ). Two black  
 646 bars indicate the inferred aseismic barrier locations.



647

648 **Figure 4.** (a) Compilation of slips at different stages as labeled (this study and Socquet et al.,  
 649 2017). Larger dots are repeaters (Meng et al., 2015). (b) Same as (a) but with interseismic  
 650 locking (Métouis et al., 2016) and seismic (white) and aseismic (green) slip events. Preseismic (2  
 651 – 3 weeks) slip is drawn as seismic slip because ~65% of moment release was released  
 652 seismically (Socquet et al., 2017). Latitudinal range of inferred aseismic barriers is shown with  
 653 two light blue bars. See Figure 3 for other elements.

654

655

656

657

658

659

660

**Largest aftershock nucleation driven by afterslip during the 2014 Iquique sequence**

Yuji Itoh<sup>1,2</sup>, Anne Socquet<sup>1</sup>, and Mathilde Radiguet<sup>1</sup>

<sup>1</sup>Univ. Grenoble Alpes, Univ. Savoie Mont Blanc, CNRS, IRD, Univ. Gustave Eiffel, ISTerre, 38000 Grenoble, France.

<sup>2</sup>Earthquake Research Institute, The University of Tokyo, Tokyo, Japan.

**Contents of this file**

Text S1 to S4  
Table S1  
Figures S1 to S24

**Text S1. Details of GPS data cleaning**

We employed 5-minute high-rate GPS coordinates processed by Nevada Geodetic Laboratory (NGL; Blewitt et al., 2018). These coordinates are estimated by a Kalman filter and smoother with a random walk parameter of 17 m over the 5-minute interval (Blewitt et al., 2018; <http://geodesy.unr.edu/gps/ngl.acn.txt> and [http://geodesy.unr.edu/gps\\_timeseries/QA.pdf](http://geodesy.unr.edu/gps_timeseries/QA.pdf); last accessed on 01 September 2023). Hence, forward and backward propagation of the rapid position changes due to the mainshock and the largest aftershock to the interevent and the post-largest-aftershock stages should be minimal. Also, NGL processes 5-min coordinates during each day individually and there is no additional smoothing or other treatment applied to coordinates near each day boundary (Blewitt et al., 2018). The mainshock and the largest aftershock occurred at 23:46:45.72UTC on 1 Apr 2014 and 02:43:13.94UTC on 3 Apr 2014, respectively (Soto et al., 2019a), so coordinates during 24 hours of the 27-hour interevent stage are individually processed and hence are free from the offsets of the two earthquakes. Therefore, we concluded that the interevent deformation found in this study is not a technical artifact of GPS processing.

We removed spatiotemporally correlated fluctuations in 5-minute coordinates through the following procedure (mostly the same as Moutote et al., 2023). First, we fixed the GPS coordinates into the South American plate using a plate motion model with respect to ITRF2014 (Altamimi et al., 2007) (black in Figure S1). Then, we removed coordinate fluctuations due to multipath (e.g., Bock et al., 2000; Itoh & Aoki, 2022; Ragheb et al., 2007). Multipath signals are known to appear periodically but are usually not sinusoidal, so we estimated them using Seasonal-Trend decomposition using LOESS (STL) (Cleveland et al., 1990; Pedregosa et al., 2011) which decomposes time series into trend, periodic (termed seasonal in the program), and residual terms. We regard the periodic term as an estimation of multipath signals and, hence, we chose 86100 seconds (23 hours 55 minutes) for the period because it is the integer multiple of the sampling interval closest to the typical multipath period (86154 seconds or 23 hours 55 minutes 54 seconds; Ragheb et al., 2007). We removed only the estimated periodic component and kept the other two terms for the subsequent analysis (red in Figure S1). Next, we removed diurnal variation in the data, using the same approach for the multipath removal but with a period of 86400 seconds (1 day; Itoh et al., 2022) (pink in Figure S1). Next, we removed common mode error which originates from the fluctuation of the reference frame and satellite orbit errors (Wdowinski et al., 1997), which is estimated in the following procedure.

We extracted common mode error by stacking time series at 6 sites in the nodal direction of the mainshock and aftershock, where little coseismic deformation is expected (Figure 1 and orange in Figure S1). Before stacking them, the time series at these sites went through the same noise removal procedure elaborated above and then we further removed outliers and a linear trend of time series at each site. The outliers are defined as epochs satisfying the following criterion (Equation (S1)) (Itoh et al., 2022);

$$\left| u_i - \frac{q_1 + q_3}{2} \right| > n * \frac{q_3 - q_1}{2} \quad (\text{S1})$$

where,  $u_i$  is the displacement at the  $i$ -th epoch,  $q_1$  and  $q_3$  are the 25 and 75 percentile values of the position time series, respectively, derived from data between 60 days before and 30 days after the day of the mainshock. The term  $n$  is a threshold controlling how strict or loose we impose the outlier criterion and we adopted  $n = 8$  in this study based on trial-and-error approaches. We estimated and removed the linear trend from the data after this outlier removal step.

### **Text S2. The trajectory model fit procedure and error evaluation of retrieved displacements**

We retrieved surface deformation at the four stages from the following trajectory model fit result with Equation (S2) (Figures 1b-e, S2a-d, and S8a-f).

$$x(t) = a + \left\{ b + c \log \left( 1 + \frac{t-t_0}{a} \right) \right\} H(t - t_0) + \left\{ e + f \log \left( 1 + \frac{t-t_1}{g} \right) \right\} H(t - t_1) \quad (\text{S2})$$

where  $a$ ,  $b$ , and  $e$  are the initial position and coseismic offsets of the mainshock (at time  $t = t_0$ ) and the largest aftershock (at  $t = t_1$ ), respectively. The first and second logarithmic terms model postseismic responses assuming velocity-strengthening afterslip (Marone et al., 1991; Perfettini & Avouac, 2004; Perfettini et al., 2018) induced by the

mainshock and the largest aftershock, respectively. Different functions (Marill et al., 2021; Periollat et al., 2022) did not significantly improve the fit. We determined the amplitude of each term by the least square regression. Coseismic displacements of the two quakes (Figures S10a-b, S10d-e, and S15) are from the step terms (i.e.,  $b$  and  $e$ ) while displacements during the two interevent and the post-largest-aftershock stages are increment of the model prediction for the time window of interest (Figures 1b, S2d, S8c, S8f, and S10-S11). The search range for  $d$  and  $g$  in Equation (S2) is 0.1 – 3 and 0.1 – 10 days, respectively (Figure S3). For sites north of 19°S, we excluded the term relating to the largest aftershock (i.e., the third term of Equation (S2)) and set the search range for  $d$  as 0.1 – 10 days by considering the largest aftershock size and the great hypocenter distance.

We applied this trajectory model to fit the cleaned time series twice to remove outliers. We used Equation (S1) in both of the two fitting steps, but, after the first fit, we removed outliers defined as epochs which deviate from the model prediction by 3 times post-fit RMS (Figure S4) because the time series of the sites in the main region of interest have not yet gone through the outlier removal using Equation (S2). RMS is here defined as

$$RMS = \sqrt{\frac{\sum_{i=1}^n \left( \frac{o(t_i) - x(t_i)}{w(t_i)} \right)^2}{\sum_{i=1}^n \frac{1}{w(t_i)^2}}} \quad (S3)$$

Where,  $o(t_i)$  and  $w(t_i)$  are a coordinate and its error at  $t = t_i$ , respectively and  $n$  is the number of available epochs. Then, we again fit the same function to the data without the outliers. We preferred to employ the classical  $3 * RMS$  criterion of Equation (S3) than Equation (S1) to define the outliers at the main sites of interest after obtaining the residual of the first fit because we carried out the least square trajectory model fit. However, we admit that there would be no strong superiority in our choice of Equation (S3) over Equation (S1).

For simplicity, formal displacement errors of the coseismic displacements are obtained by the linear least-square transformation of the GPS position observation errors while formal errors of the displacements during the two aseismic stages were defined as Equation (S3) but with the time windows of each stage.

### **Text S3. Details of the moving median analysis**

We derived the moving median (Figures 2a-b) from the data after removing the mainshock and largest-aftershock coseismic steps determined by the trajectory model fit. We did not exclude the pre-mainshock or post-largest-aftershock coordinates for deriving moving median values the first or last 0.25 days because, given the definition of median, distortion of the obtained moving median should be limited. Using a shorter window length by excluding the pre-mainshock or post-largest-aftershock coordinates from the calculation ended up underestimating the rapid transient deformation at the very beginning of the interevent stage (Figure S22). We computed displacements during the two interevent substages and the whole interevent stage by simply taking the difference of coordinates (Figures 2e-f and S17). For simplicity, their formal errors are taken from the trajectory analysis results (See Text S2).

#### **Text S4. Inversions of incremental interevent displacements derived from the motogram analysis**

For the interevent afterslip, we used four different datasets, namely, (i) the cumulative interevent displacements derived from the trajectory model fit (i.e., Equation (1); Figures 1b, 3a, and S2d-e), (ii) same as (i) but displacements derived from the moving median (Figures S17a-b), (iii) displacements during the first interevent substage, derived from the moving median (Figures 2e and S17c) and (iv) same as (iii) but during the second interevent substage (Figures 2f and S17d).

For inversions of the interevent afterslip with the datasets derived from the moving median analysis (i.e., Datasets (ii), (iii), and (iv); Figures 2e-f and S17), we excluded GPS sites located north of 19°S, namely those near the border of Chile and Peru, because including them highly destabilized the slip inversion (Figures S23-S24). Furthermore, to obtain the consistent slip pattern in all the interevent slip models, we added a constraint to the upper bound of the slip amplitude (Figures S23-S24). For the cumulative slip inversion with Dataset (ii), the upper bound is set to those obtained by the inversion of displacements obtained by the trajectory model fit (i.e., Dataset (i); Figure 3a). The obtained slip amplitude was subsequently used as the upper bound of slip amplitude (Figures S17a-b) during the first and second interevent substages with the datasets (iii) (Figures 2e and S17c) and (iv) (Figures 2f and S17d). For the reason of practical implementation, we did not require the sum of slip or moment at each subfault at the two substages to be equal to those derived from the whole period dataset (i) or (ii). The sum of the moments at the two substages is slightly smaller than the inversions at the whole period (Table S1; Figure S14).

#### **Text S5. Coulomb stress change calculation**

We computed coulomb stress change (CSC) associated with the mainshock and the interevent aftershock (Figure S9). CSC is defined as follows.

$$CSC = \Delta\tau + \mu\Delta\sigma \quad (4)$$

where,  $\Delta\tau$  and  $\Delta\sigma$  indicate elastic shear and normal stress change induced by slip, respectively. Positive  $\Delta\tau$  is taken in a hypothetical slip direction of receiver fault defined as the convergence direction of Nazca and South American plates. Positive  $\Delta\sigma$  is taken in an unclamping direction. The term  $\mu$  is a static effective frictional coefficient which was set to 0.4.

**Table S1. Geodetic, seismic, and aseismic moments and equivalent moment magnitude ( $N m / M_w$ ) evaluated in this study at the interevent stage.**

	Interevent total <sup>c</sup>	Interevent total <sup>d</sup>	1 <sup>st</sup> substage <sup>e</sup>	2 <sup>nd</sup> substage <sup>f</sup>
The entire model region				
Geodetic	9.0*10 <sup>19</sup> / 7.2	7.9*10 <sup>19</sup> / 7.2	5.7*10 <sup>19</sup> / 7.1	1.5*10 <sup>19</sup> / 6.7
Seismic <sup>a</sup>	2.4*10 <sup>18</sup> / 6.2	Same as left	5.4*10 <sup>17</sup> / 5.8	1.8*10 <sup>18</sup> / 6.1
Aseismic <sup>b</sup>	8.9*10 <sup>19</sup> / 7.2	7.8*10 <sup>19</sup> / 7.2	5.6*10 <sup>19</sup> / 7.1	1.4*10 <sup>19</sup> / 6.7
The mainshock latitude (referred to as "North")				
Geodetic	7.2*10 <sup>19</sup> / 7.2	6.3*10 <sup>19</sup> / 7.1	4.6*10 <sup>19</sup> / 7.0	1.1*10 <sup>19</sup> / 6.6
Seismic <sup>a</sup>	5.2*10 <sup>17</sup> / 5.7	Same as left	4.8*10 <sup>17</sup> / 5.7	4.1*10 <sup>16</sup> / 5.0
Aseismic <sup>b</sup>	7.1*10 <sup>19</sup> / 7.2	6.3*10 <sup>19</sup> / 7.1	4.5*10 <sup>19</sup> / 7.0	1.1*10 <sup>19</sup> / 6.6
The largest aftershock latitude (referred to as "South")				
Geodetic	1.8*10 <sup>19</sup> / 6.8	1.6*10 <sup>19</sup> / 6.7	1.1*10 <sup>19</sup> / 6.6	4.8*10 <sup>18</sup> / 6.4
Seismic <sup>a</sup>	1.8*10 <sup>18</sup> / 5.7	Same as left	5.9*10 <sup>16</sup> / 5.1	1.8*10 <sup>18</sup> / 6.1
Aseismic <sup>b</sup>	1.6*10 <sup>19</sup> / 6.7	1.6*10 <sup>19</sup> / 6.7	1.1*10 <sup>19</sup> / 6.6	3.1*10 <sup>18</sup> / 6.3

<sup>a</sup> Determined by the seismicity analysis with a magnitude of the event 45 minutes before the largest aftershock fixed

<sup>b</sup> Geodetic – Seismic

<sup>c</sup> Geodetic moment determined by the slip inversions of GPS data (dataset (i); Text S4)

<sup>d</sup> Geodetic moment determined by the slip inversions of GPS data (dataset (ii); Text S4)

<sup>e</sup> Geodetic moment determined by the slip inversions of GPS data (dataset (iii); Text S4)

<sup>f</sup> Geodetic moment determined by the slip inversions of GPS data (dataset (iv); Text S4)

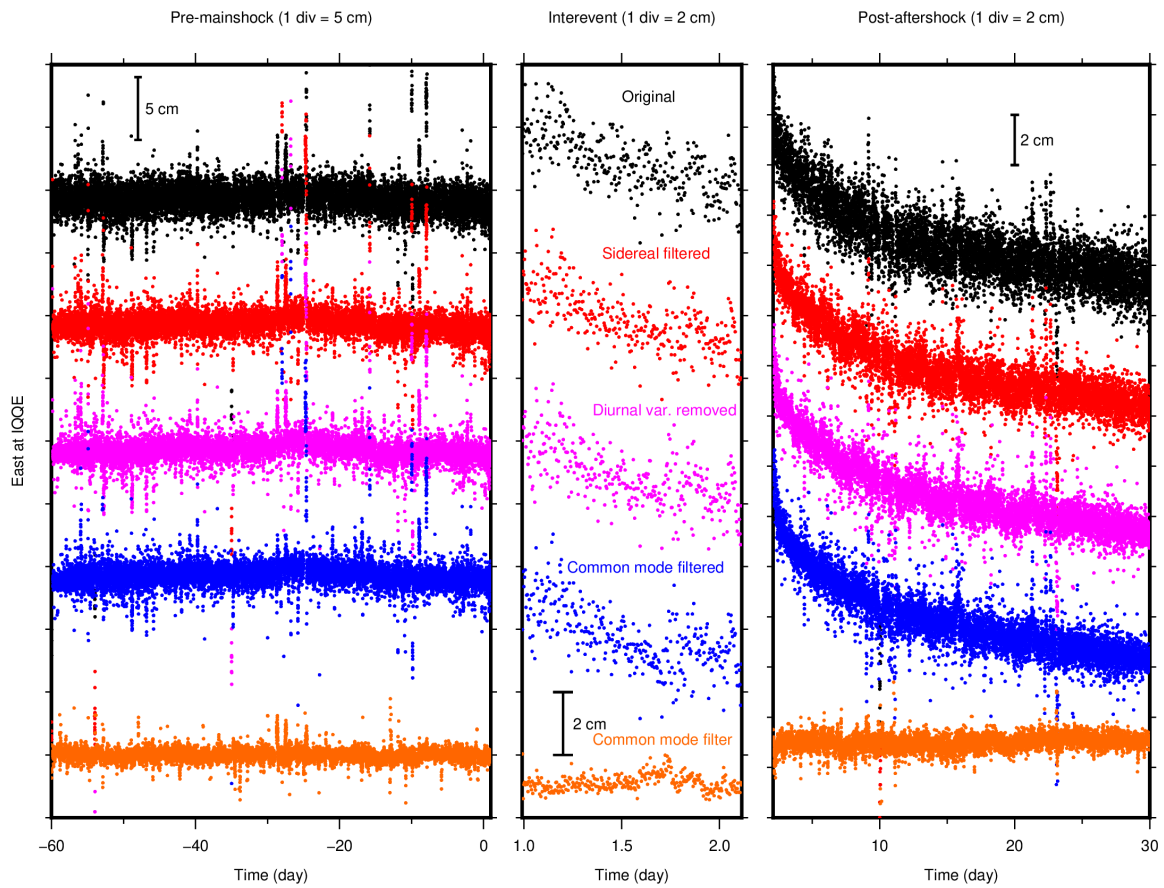


**Figure S1.** High-rate 5-min GPS data cleaning procedure (East component at IQQE as an example; Figure 1d). Time series with each color indicates the results of the cleaning procedure at each step as labeled. Coseismic steps of the mainshock and the largest aftershock are removed by breaking panels.

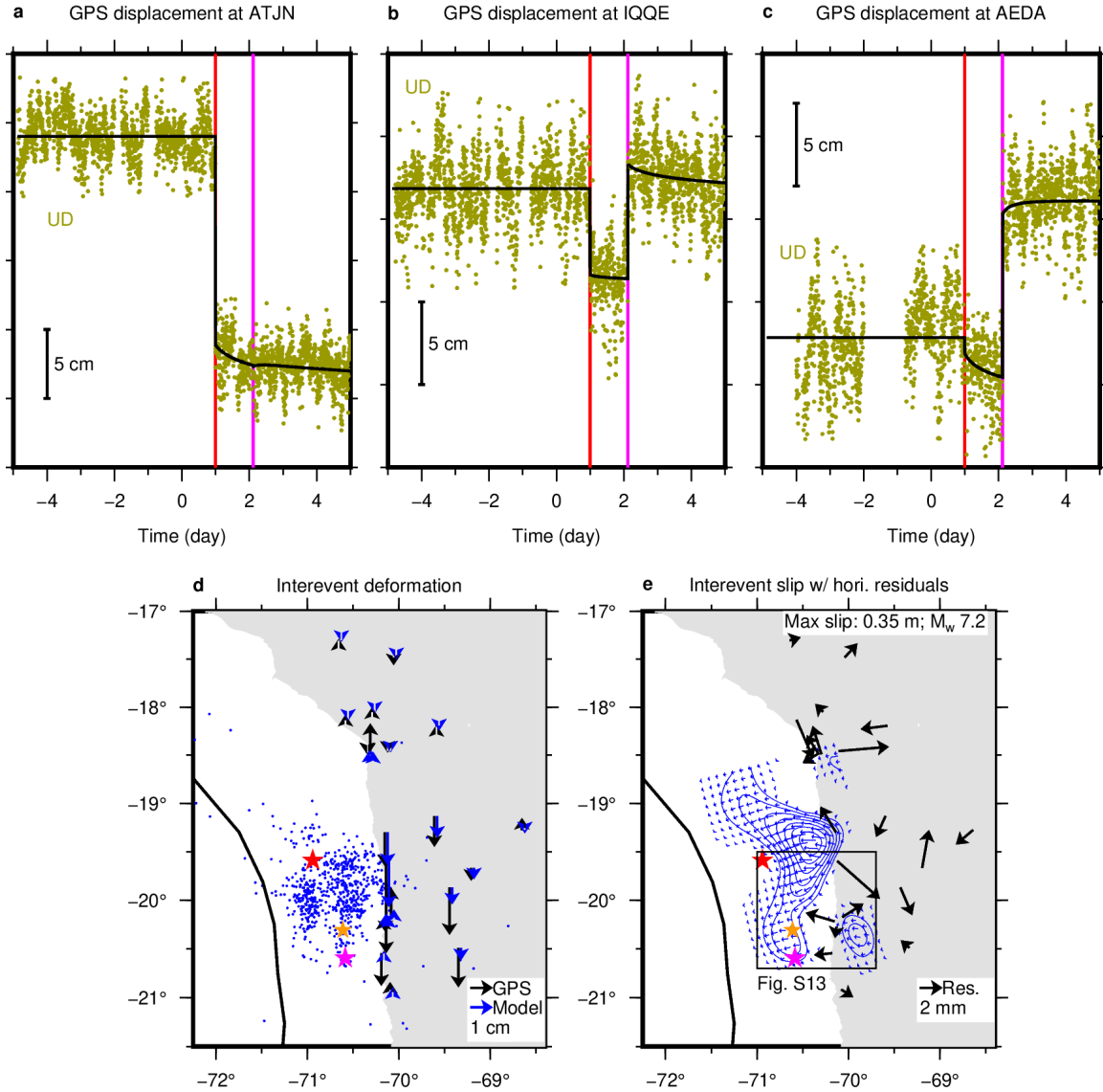


**Figure S2.** Data analysis and slip inversion result using the trajectory function fit approach. (a) – (c), Trajectory model fit results for vertical components at three sites as labeled. Location of these sites is shown in Figure 1b. (d) Vertical interevent GPS displacements (black vectors) together with model prediction (blue vectors) from aseismic slip inversion shown in (e) and Figure 2a. Refer to Figure 3 for other elements. (e) The inferred interevent slip (blue contours) with normalized slip vectors. Black vectors indicate horizontal residuals of the inversion (GPS – Model in Figure 1b).

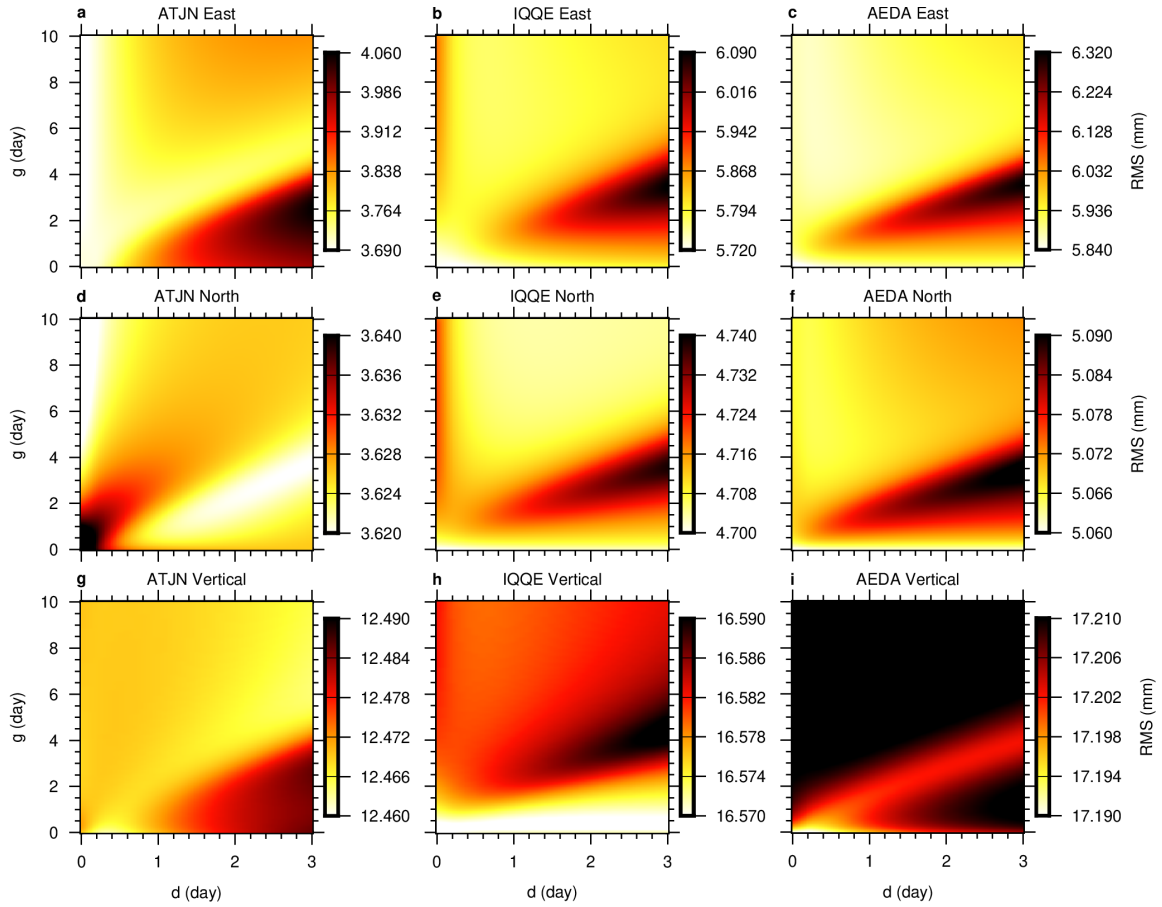


**Figure S3.** Distribution of RMS of the trajectory model fit with respect to different  $d$  and  $g$  in Equation (S2) (color). (a-c), Results for the east component at three sites as labeled. Site location is shown in Figure 1b. (d-f) and (g-i) Same as (a) – (c) but for the north and the vertical components, respectively.

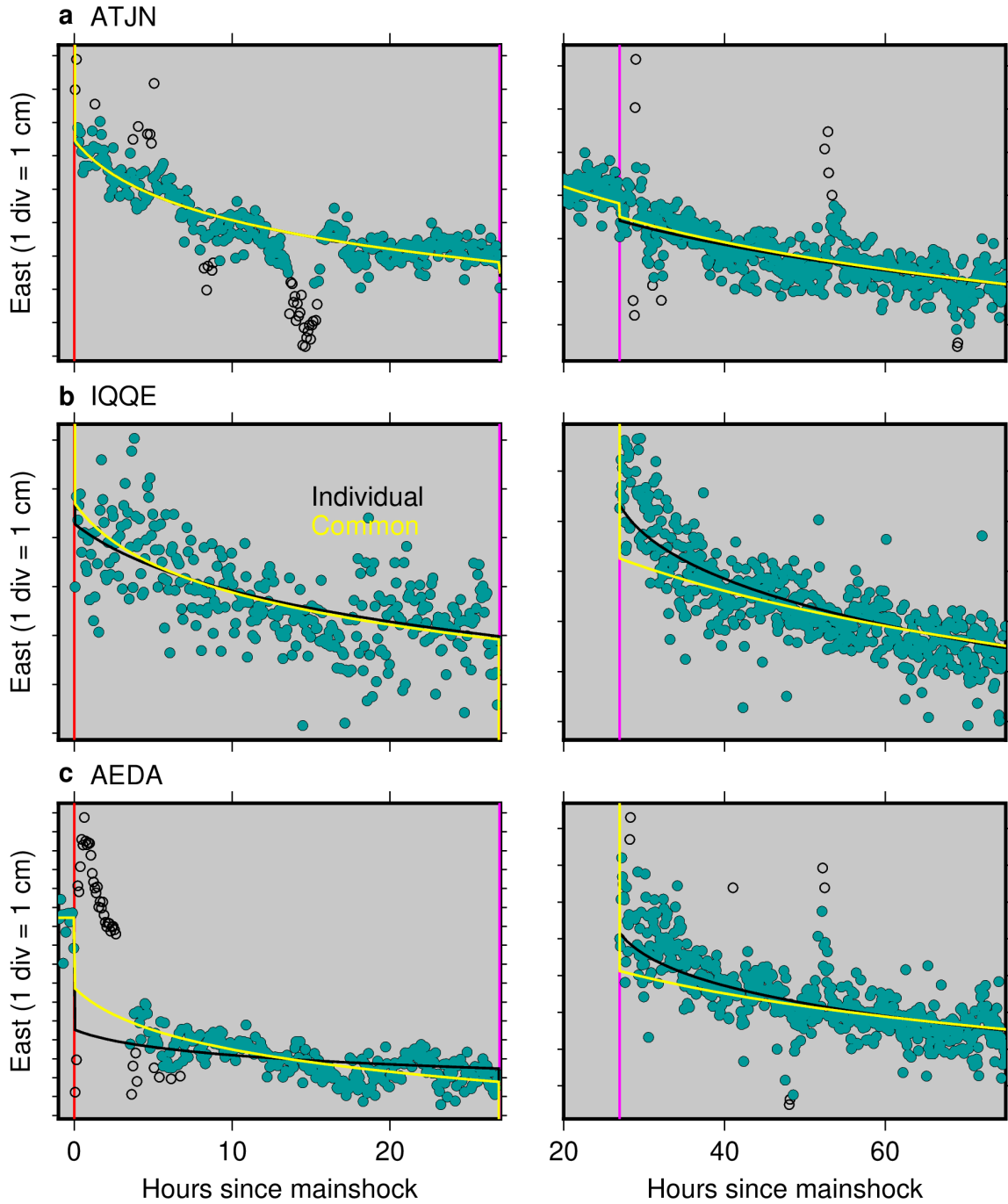


**Figure S4.** Comparison of trajectory model fit results with individual (black) and common (yellow) time constant values  $d$  and  $g$  (Equation (S2)) for all the sites and components at selected sites as labelled (locations in Figure 1b). Only the zoom-in around the mainshock and the largest aftershock time (indicated by vertical lines in red and magenta) are shown. Green and open dots indicate coordinates remained and removed by the outlier removal step after the first fit (See Text S2 for details).

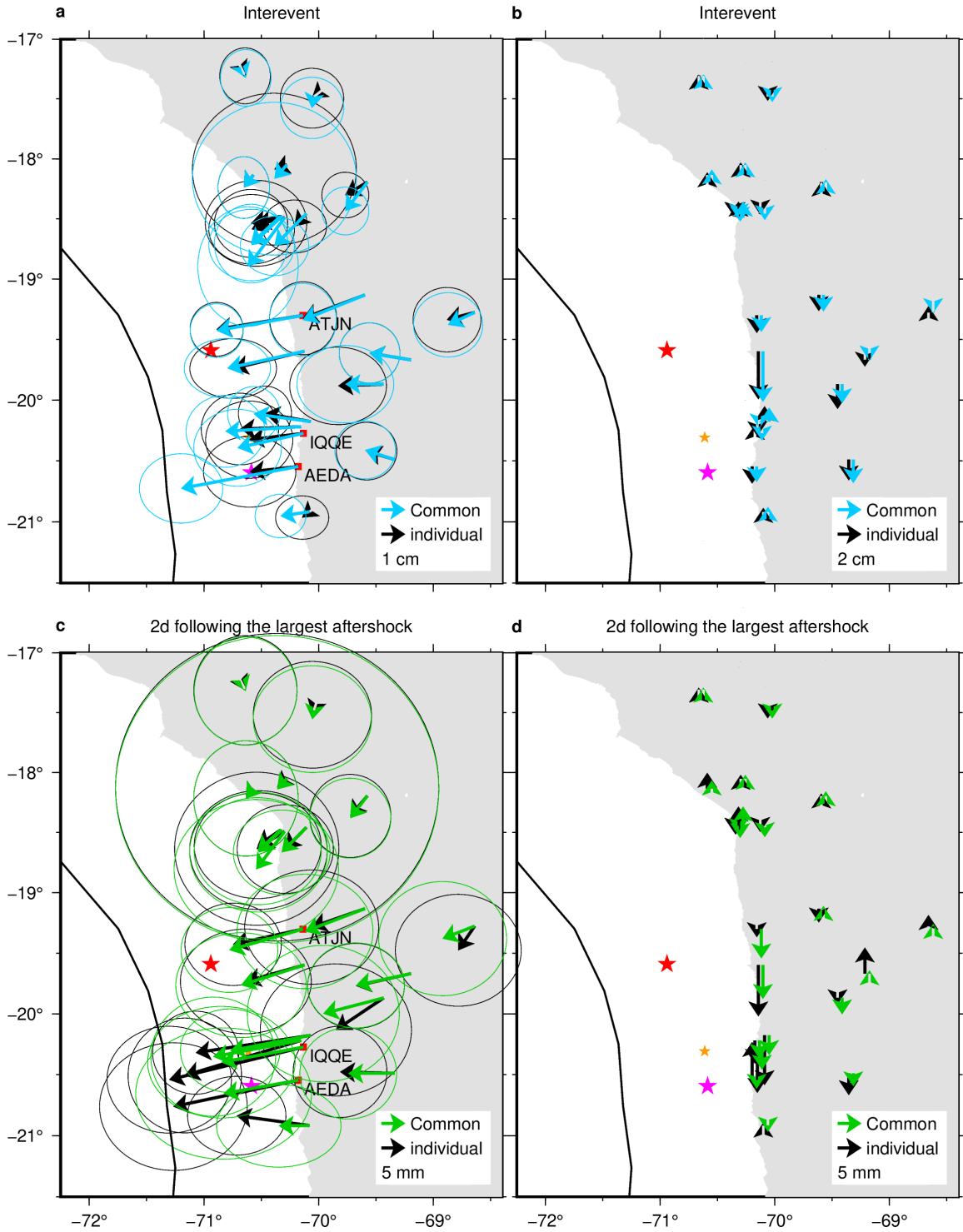


**Figure S5.** Comparison of cumulative displacements at the interevent (a: horizontal; b: vertical) and the post-largest aftershock (c: horizontal; d: vertical) stages retrieved from the trajectory model with common (light blue or green) and individual (black) time constant values  $d$  and  $g$  (Equation (S2)) for all the sites and components. The error ellipses for the vertical components are trimmed for visual clarity. Refer to Figure 1b for other elements

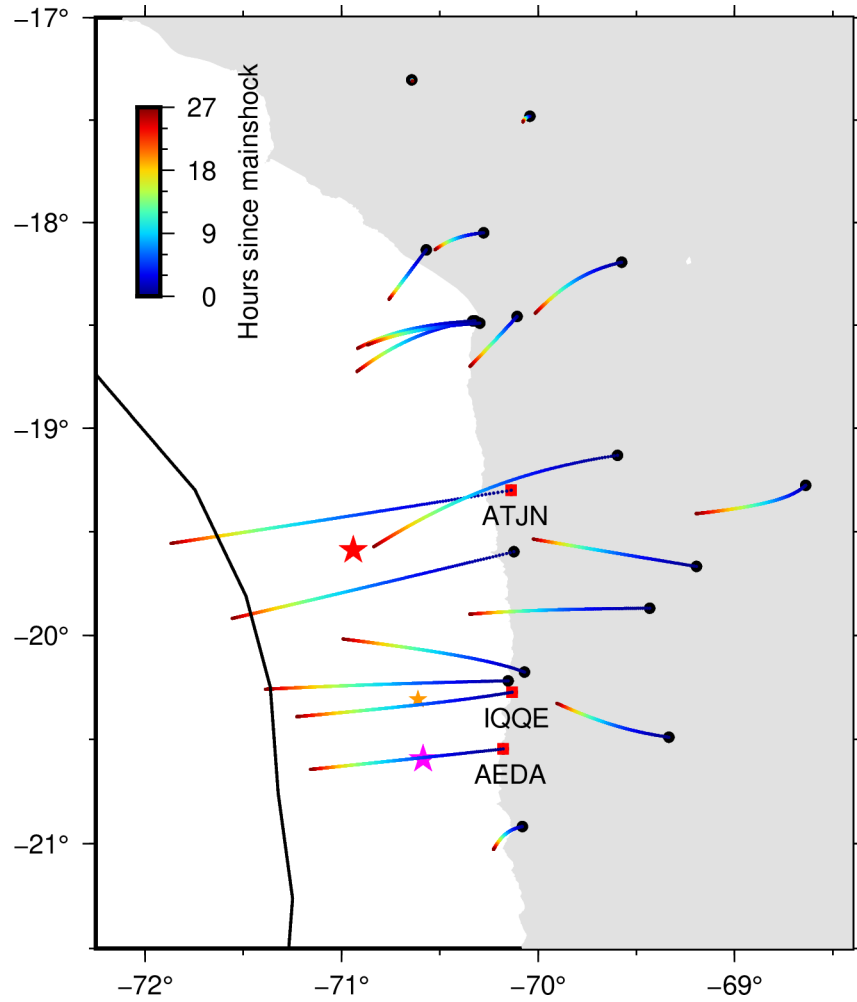


**Figure S6.** Interevent GPS site motion inferred from the trajectory model (Equation (S2)) drawn as motograms. The original time series at the three selected sites (red squares with site names) are shown in Figures 1c-e and 2b.

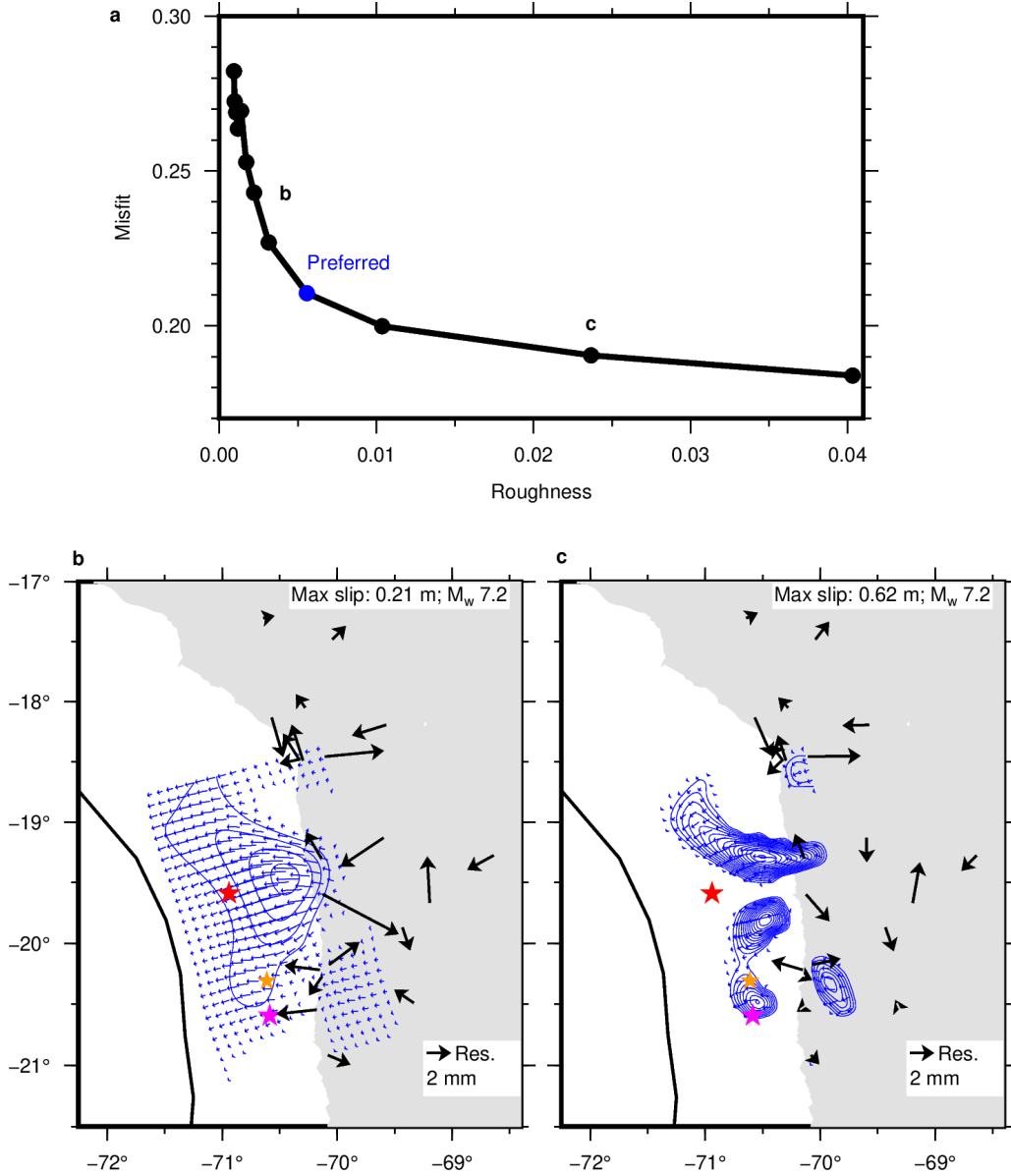


**Figure S7.** Trade-off curve of the slip roughness and misfit and model variations for the interevent slip inversion using the displacements derived from the trajectory model fit. (a) Trade-off curve. Dots indicate preferred (blue) and other tested models. (b-c), model variation with different slip roughness as shown in (a). Refer to Figure S2e for other elements.

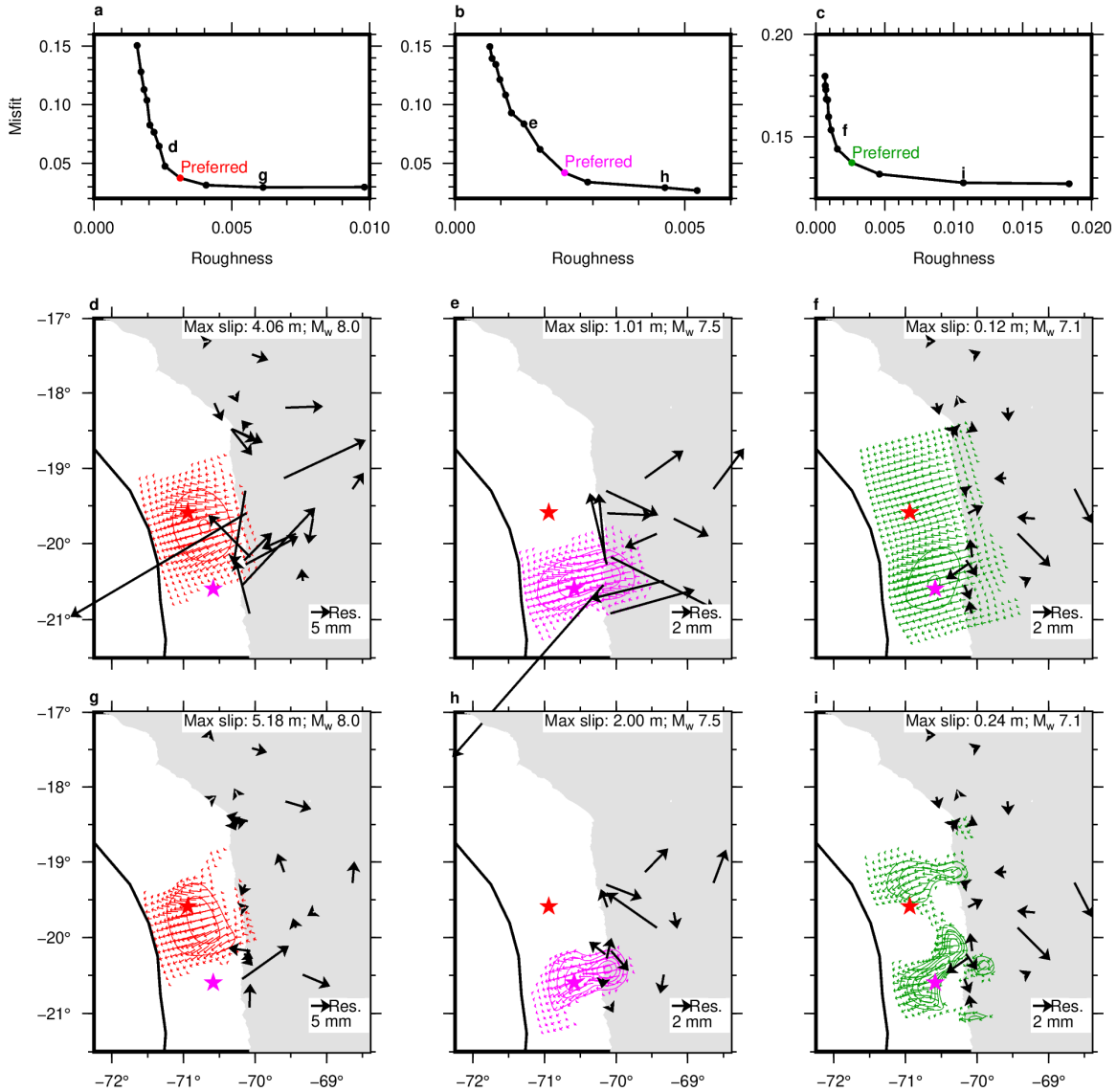


**Figure S8.** Trade-off curve of the slip roughness and misfit and model variations for the mainshock, the largest aftershock, and the post-largest-aftershock 2-day slip. (a-c) Trade-off curve for the mainshock (a), the largest aftershock (b), and subsequent 2-day afterslip (c). Dots indicate preferred (red, magenta, or green) and other tested models. (d-i) model variation with different slip roughness as shown in (a) – (c). Refer to Figures S15g-i for other elements.

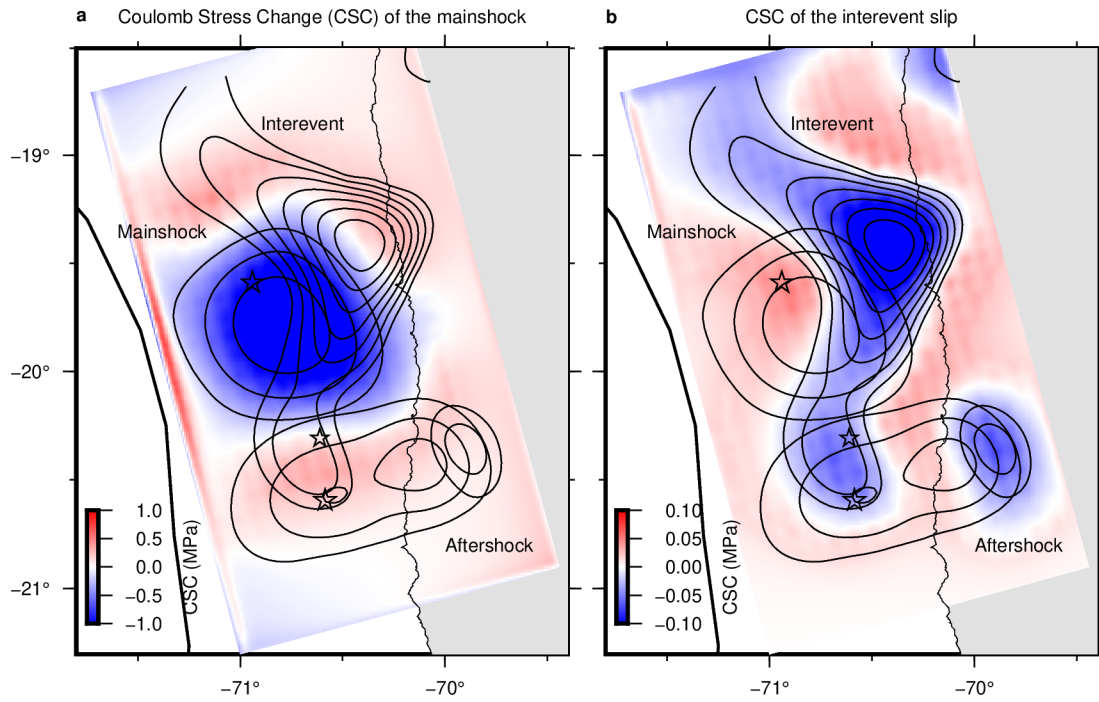


**Figure S9.** Coulomb stress change (CSC) associated with the mainshock (a) and the interevent slip (b). Solid contours are slip distribution of the mainshock, the interevent slip, and the largest aftershock, as labeled. Refer to Figure 3 for contour interval and open stars.

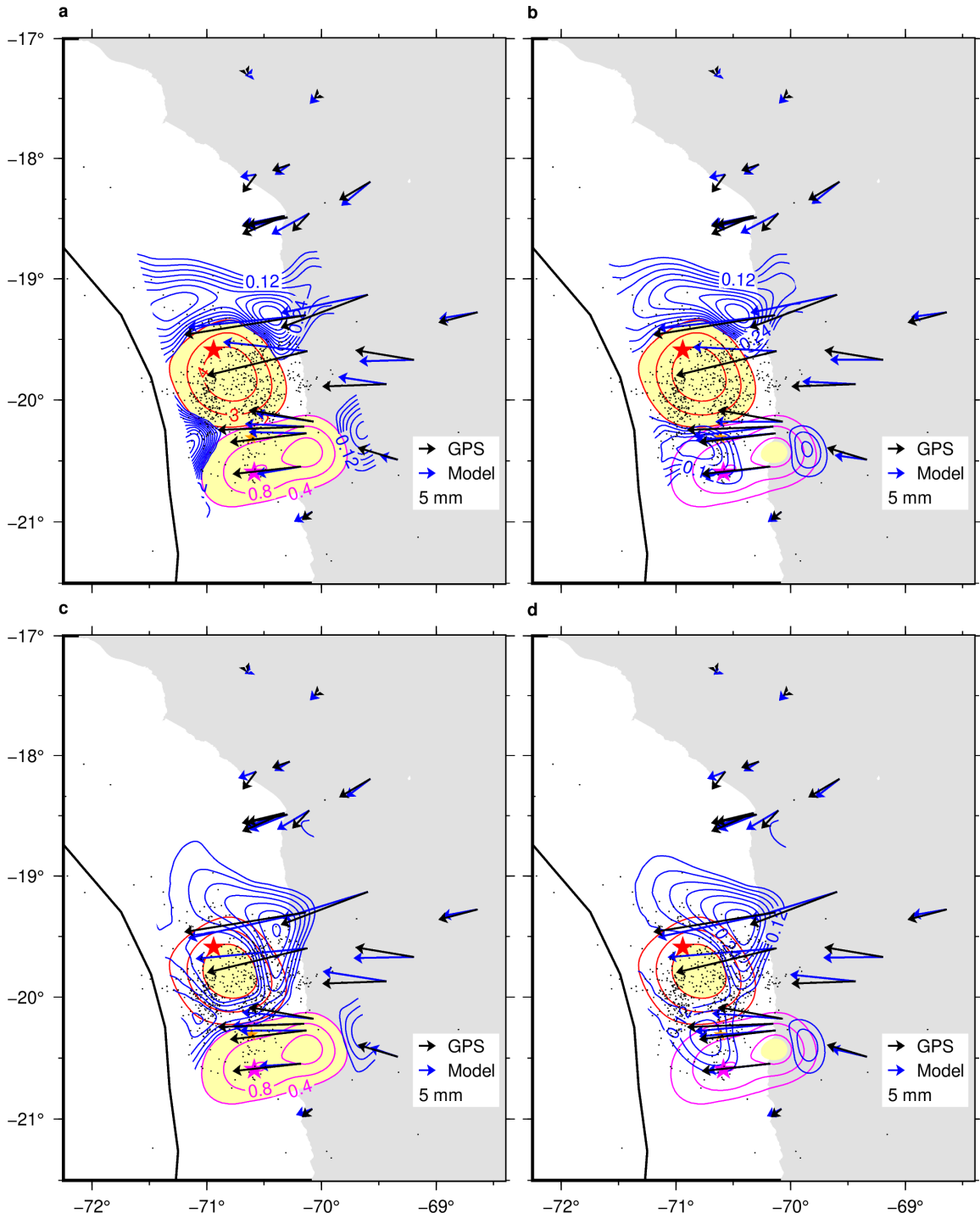


**Figure S10.** Results of interevent slip inversions (blue contours) with part of the seismic slip regions forced to have zero-slip (yellow). Black dots are the interevent seismicity (McBrearty et al., 2019). Refer to Figures 1b and 3 for other elements.

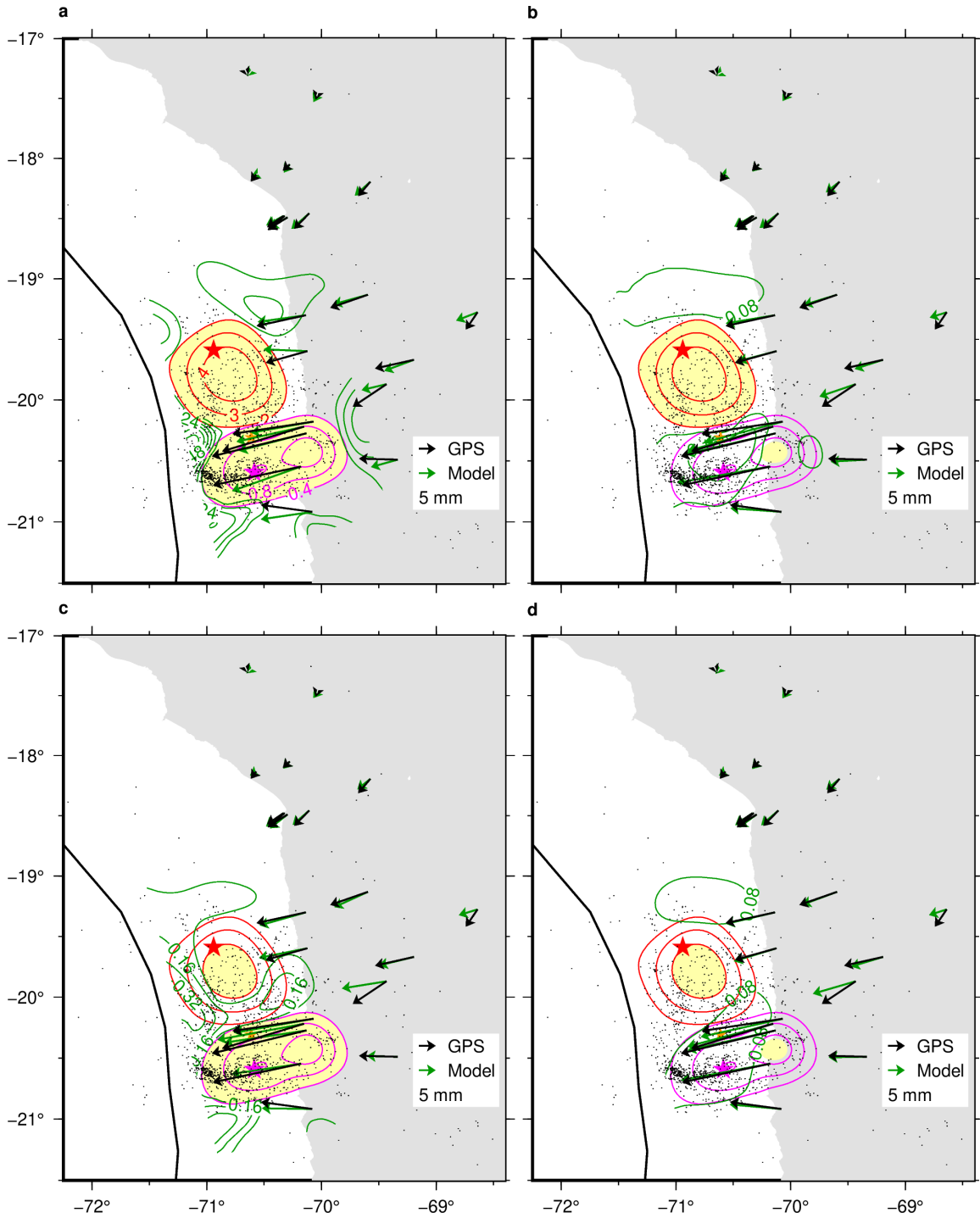


**Figure S11.** Same as Figure S10 but for the post-largest-aftershock slip for 2 days drawn in green. The black dots are the post-largest-aftershock seismicity for the 2 days. Refer to Figures 2c and 3 for other elements.

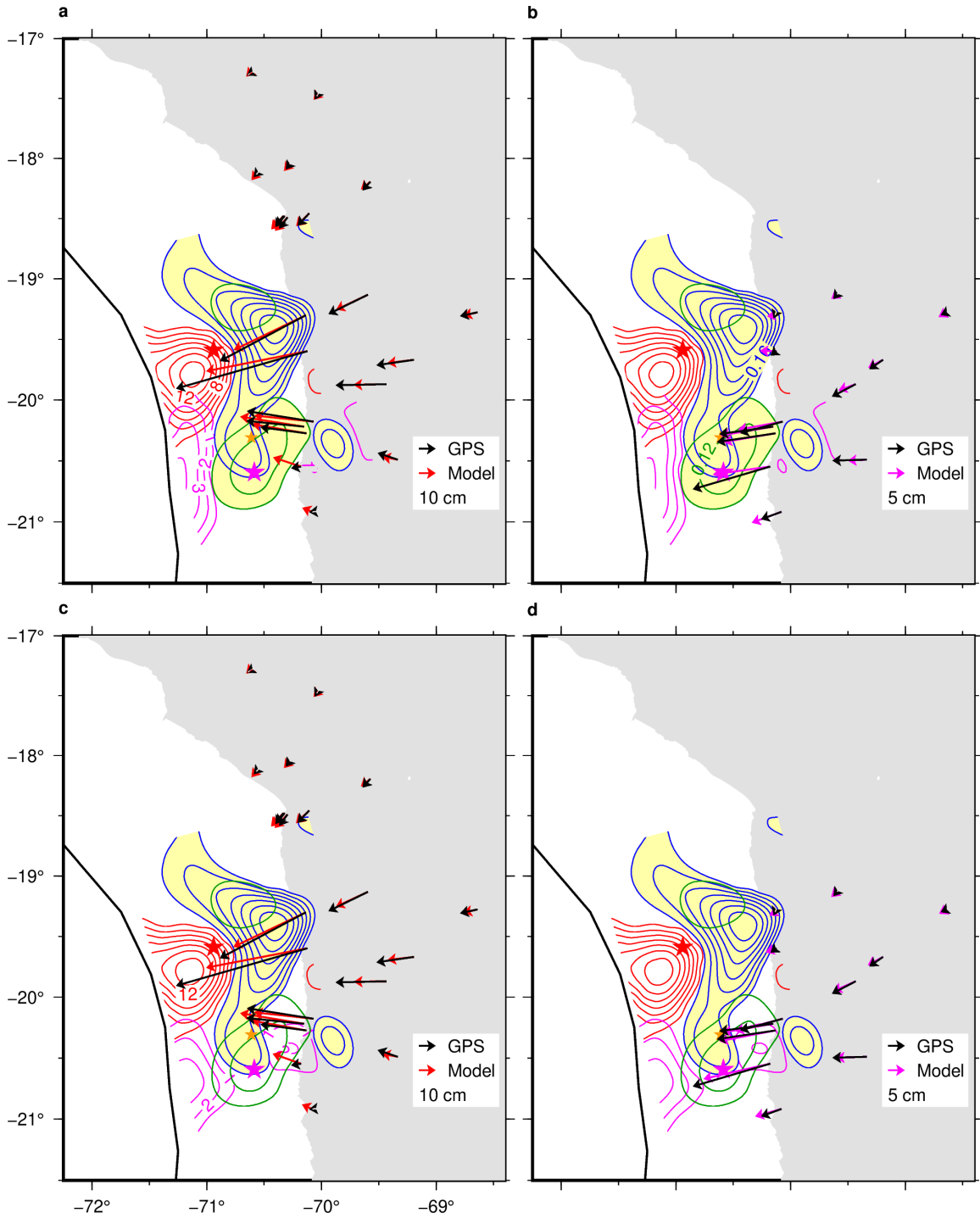


**Figure S12.** Results of coseismic slip inversions (red and magenta contours for the mainshock and the largest aftershock, respectively) with part of the interevent and post-largest-aftershock slip regions forced to have zero-slip (yellow). Refer to Figures 2a-b and 3 for other elements.

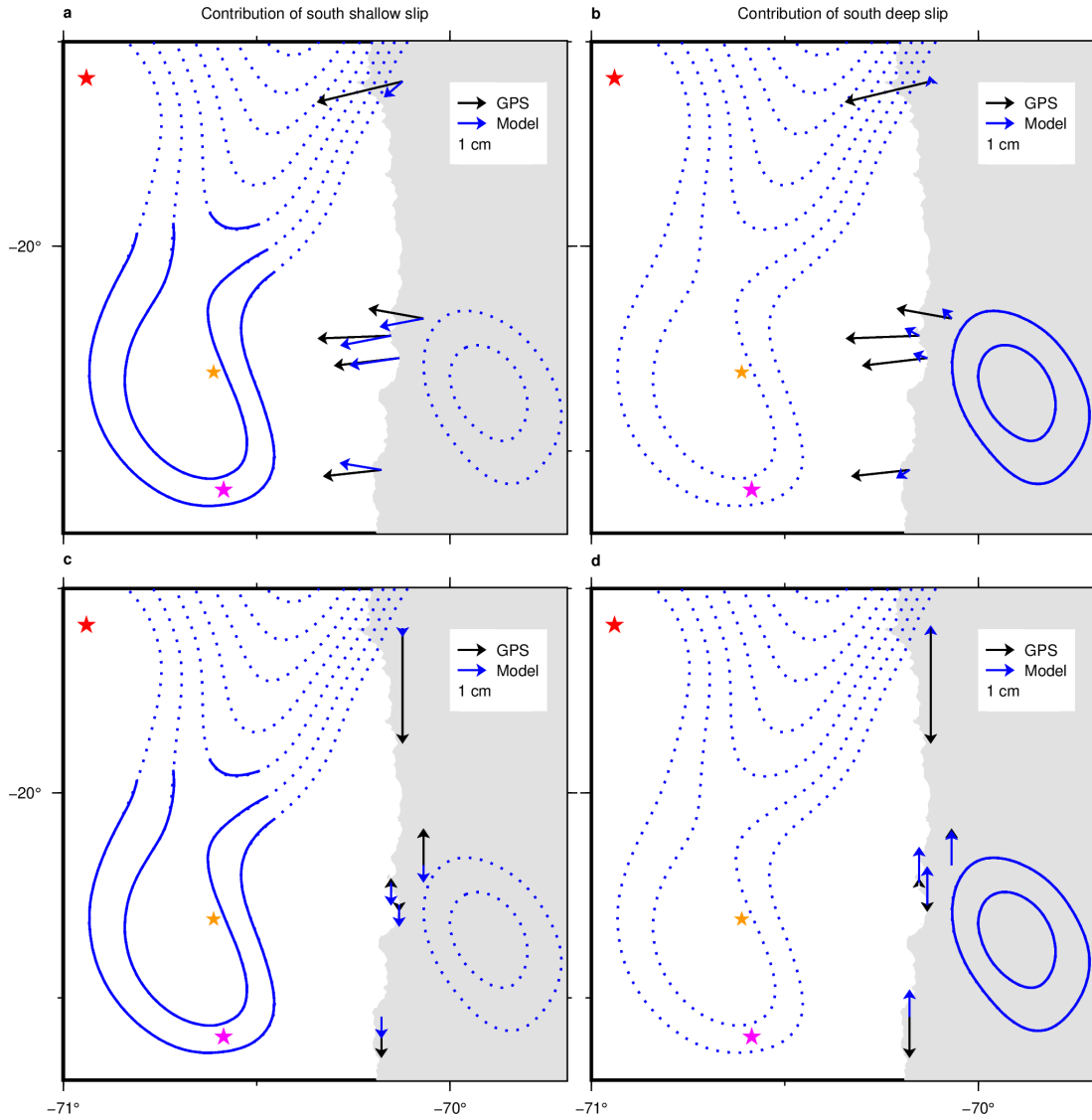


**Figure S13.** Forward modeling test results for the interevent slip. Comparison of interevent GPS displacements derived from the trajectory model fit (black) and model prediction (blue) computed from a subset (solid contours) of interevent slip inferred from the black vectors (solid + dot contours). (a-b), Comparison of horizontal displacements. (c-d) Same as (a) – (b) but for vertical displacements. Refer to Figure S2e to identify the plot area.

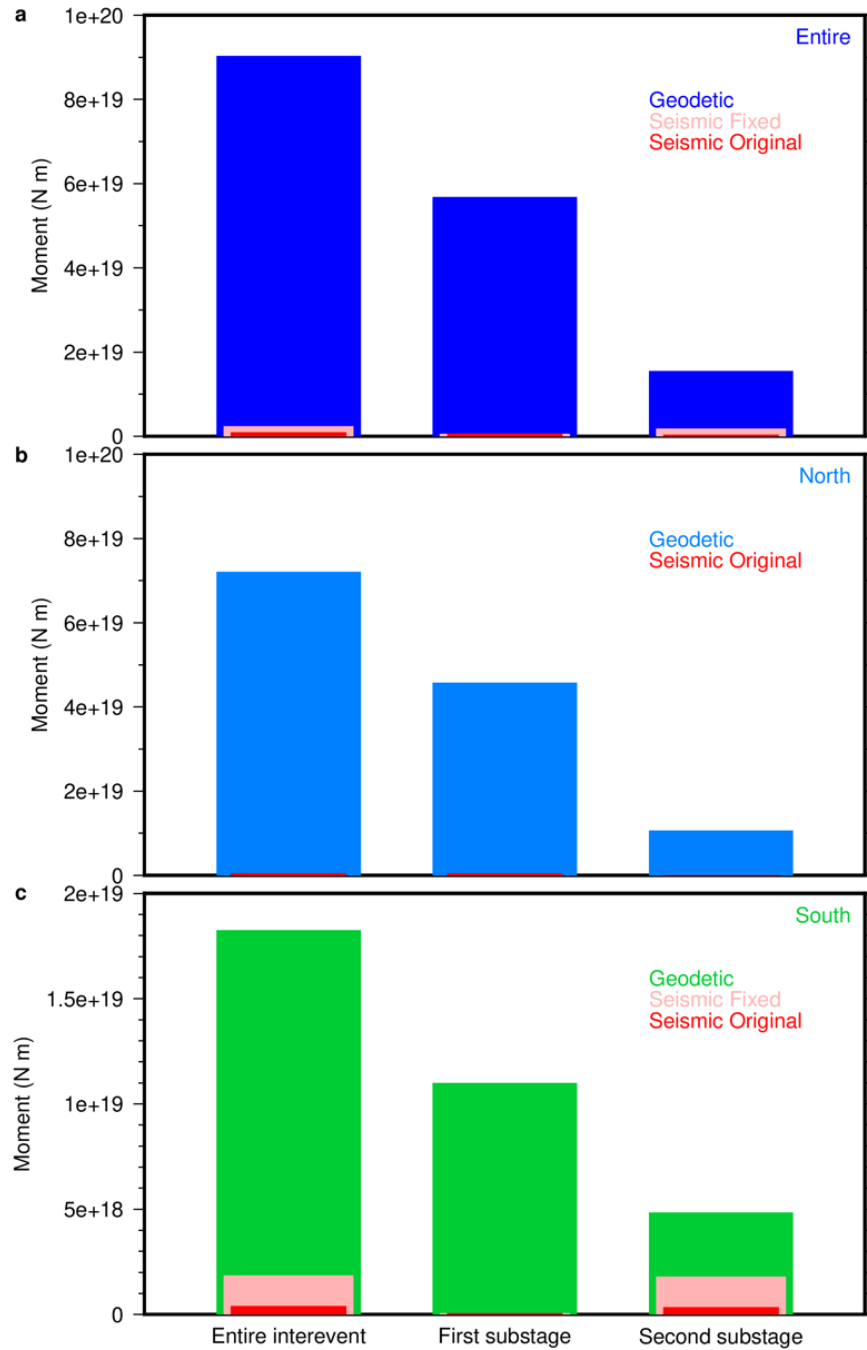


**Figure S14.** Comparison of geodetic and seismic moments during the entire interevent stage and the first and second substages as labeled in the entire (a) region and the north (b) and south (c) subregions (Table S1). The top of each bar with different colors indicates a corresponding moment value. “Seismic Fixed” means that the magnitude of the “M 6.1” event, described as M 5.6 in McBrearty et al. (2019) is fixed to  $M_w$  6.1 when calculating the seismic moment (See Main text) while “Seismic Original” is not. Geodetic moments of the entire interevent period (left) are taken from the first left column of Table S1.

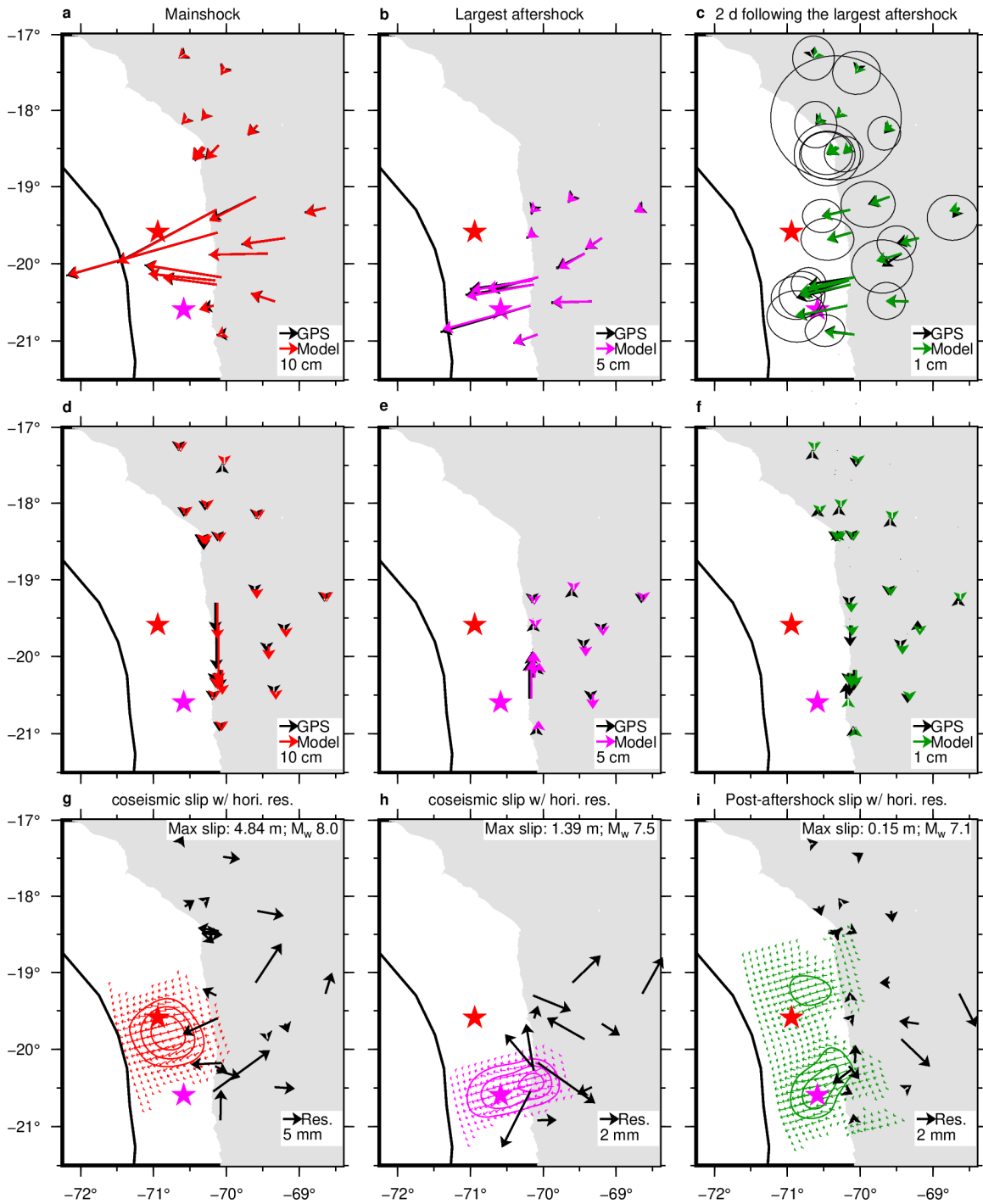


**Figure S15.** Data analysis and inversion results for the mainshock (a, d, and g), the largest aftershock (b, e, and h), and the post-largest-aftershock stage (2 days; c, f, and i). (a-c), Horizontal GPS displacements at each stage derived from the trajectory model fit. (d-f), Same as (a) – (c) but for vertical displacements. (g-i), Slip inversion results (contours) at each stage with normalized slip vectors. Black vectors indicate horizontal residuals of the inversion (GPS – Model).

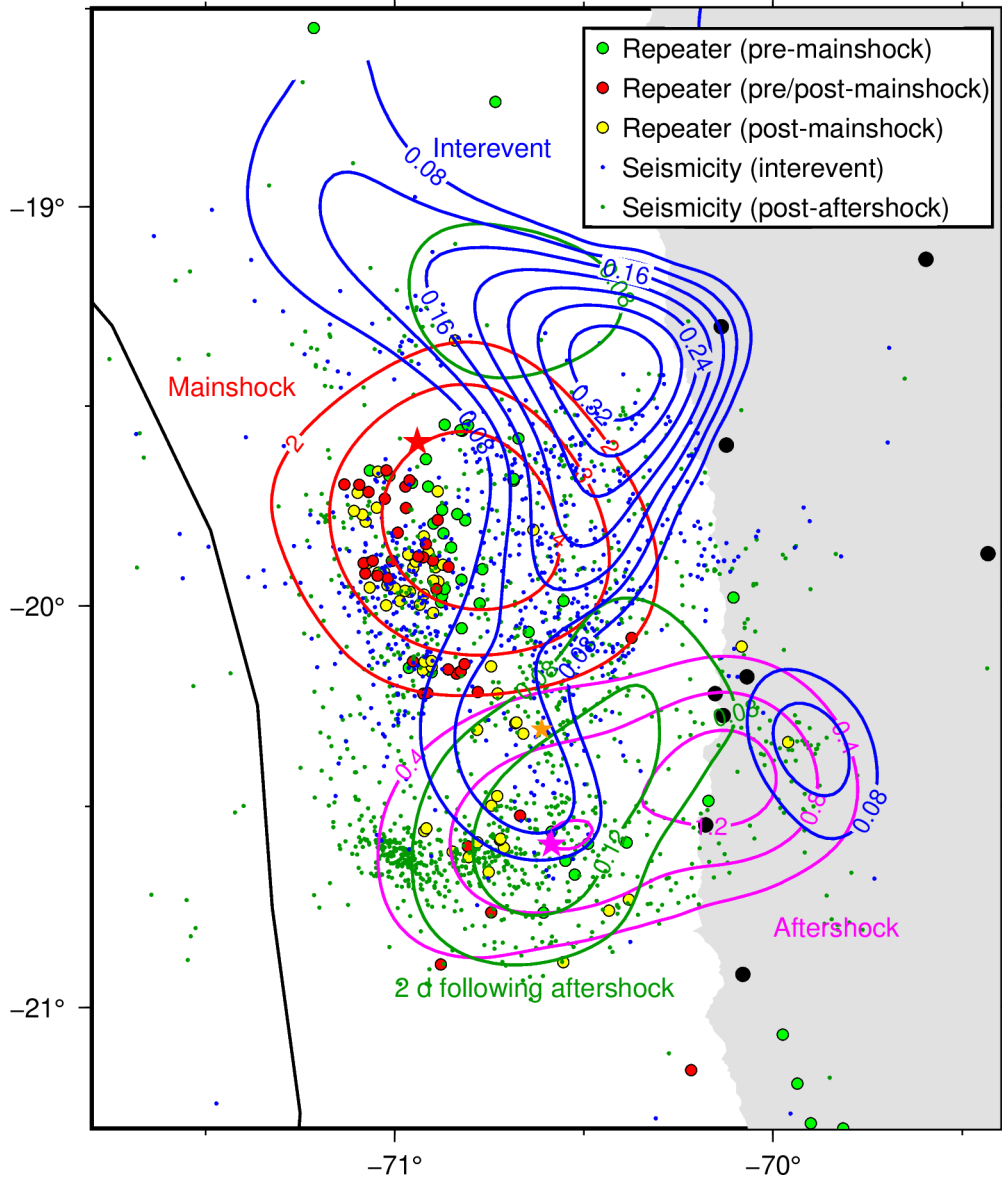


**Figure S16.** Same as Figure 3a but with the repeaters of Meng et al. (2015; Figure 4a) as labeled.

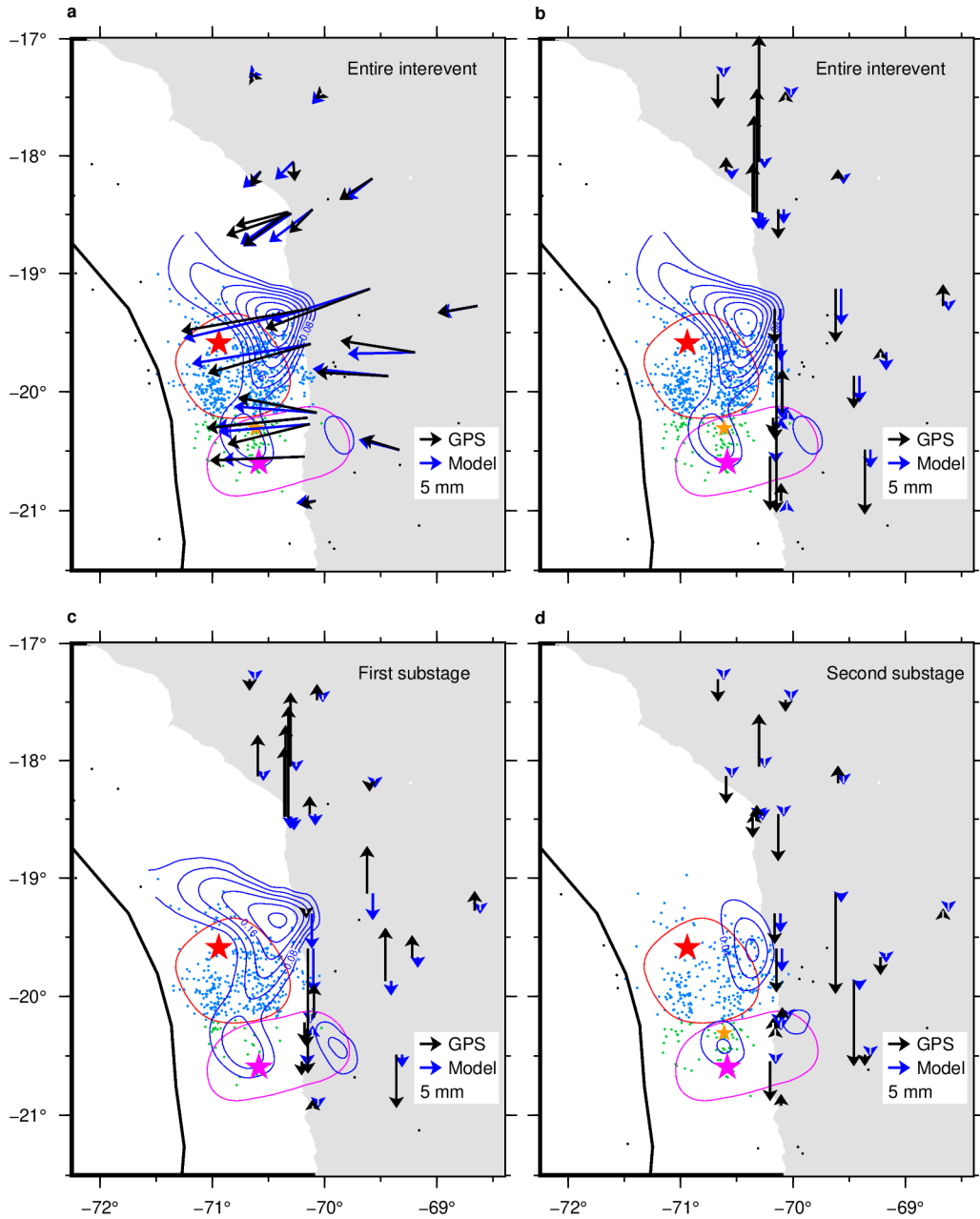


**Figure S17.** Data analysis and slip inversion result using the moving median approach. (a-b) Cumulative interevent horizontal (a) and vertical (b) displacements (black vectors) derived from the moving median analysis, together with the model prediction (blue vectors) from the inferred slip (blue contours). Refer to Figure 2 for other elements. Note that GPS displacements at sites north of 19°S are not inverted. (c-d) Same as Figures 2e-f but with vertical GPS displacements derived from the moving median analysis (black vectors) and model predictions (blue vectors).

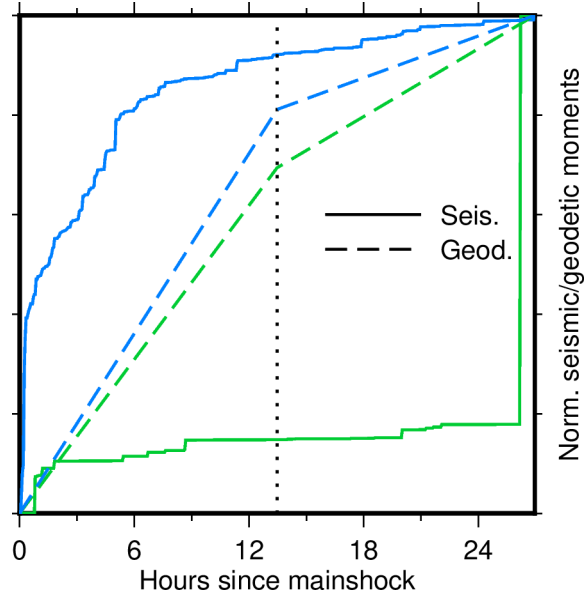


**Figure S18.** Same as Figure S2d but with the magnitude of the “M 6.1” event, described as M 5.6 in McBrearty et al. (2019) is not fixed to  $M_w$  6.1 when calculating the seismic moment (See Main text)

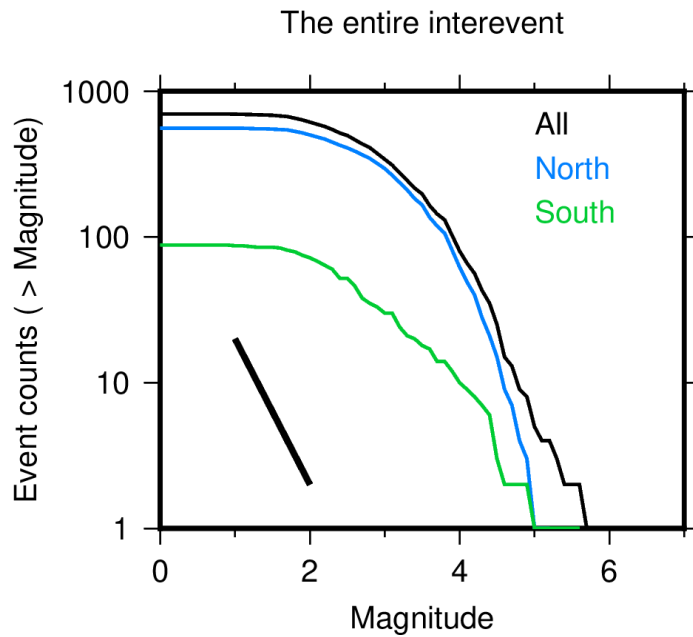


**Figure S19.** Gutenberg–Richter magnitude–count distribution curves during the interevent stage (Figure 2 and Section 2.3; McBrearty et al., 2019). Black lines indicate a slope of curves when the b-value of Gutenberg-Richter law is 1.0.

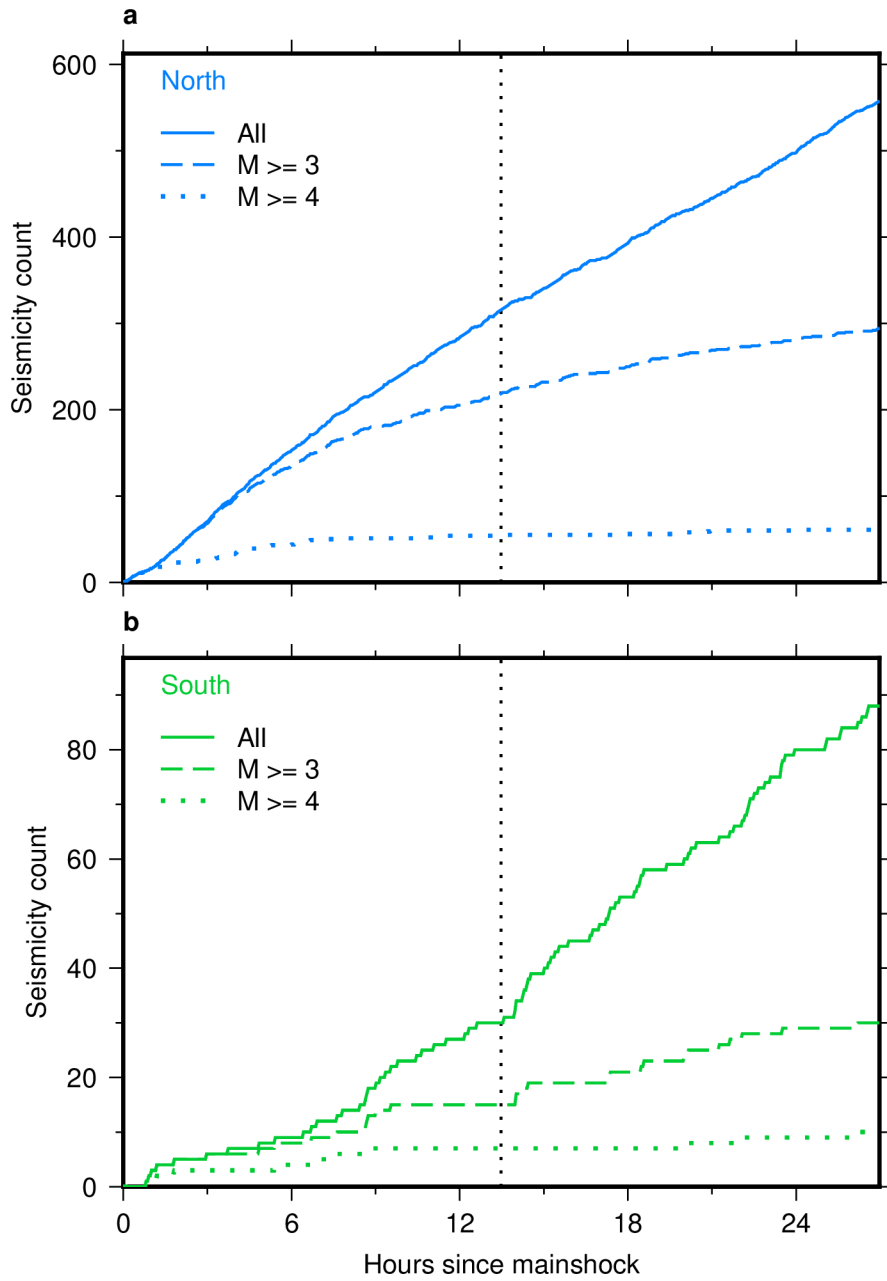


**Figure S20.** Interevent seismicity counts with all events (solid curves; same as Figure 2c) and those above magnitude 3 (broken curves) or 4 (dotted curves) in the North (a) and South (b) subregions.

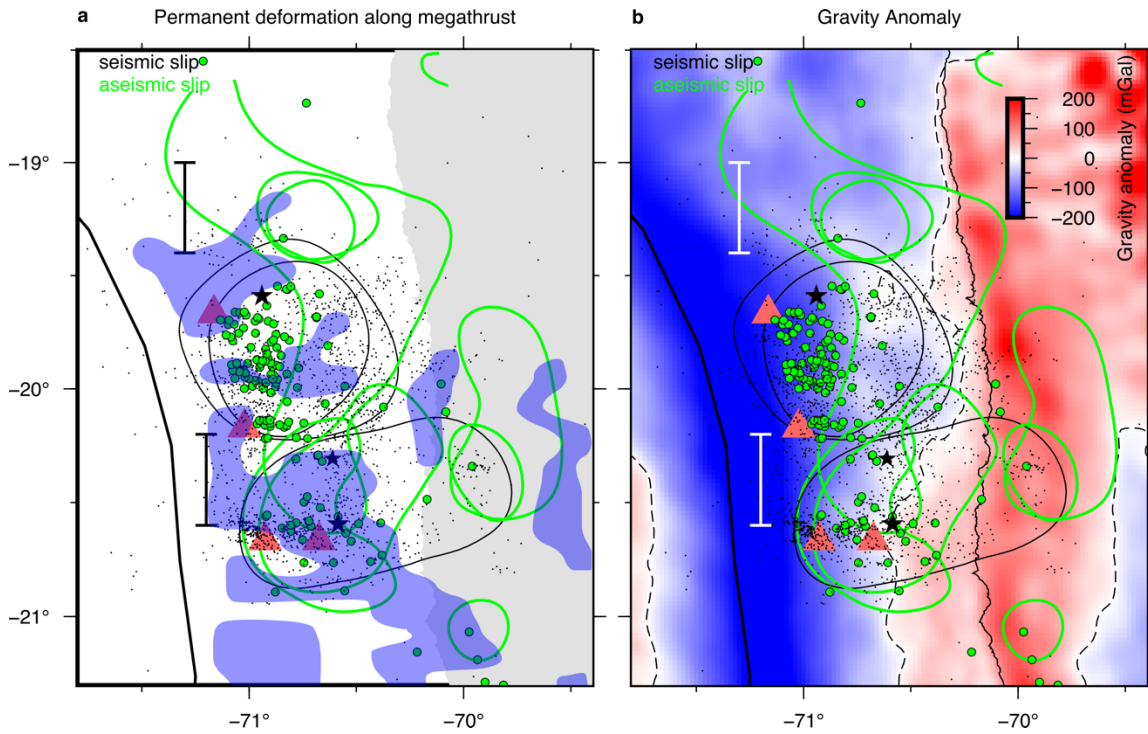


**Figure S21.** (a) Slip events at different stages with outlines of areas possibly hosting multiple faults subparallel to the megathrust (Cubas et al., 2022) (blue shapes). For clarity, seismic and aseismic slip events at different stages (Figure 4a) are drawn with black and green contours, respectively. Black dots are seismicity during the interevent and the post-largest-aftershock stages (McBrearty et al., 2019). (b) Same as (a) but with gravity anomaly (Sandwell et al., 2014) (background color) with zero value outlined with broken contours. Refer to Figure 1a for other elements.

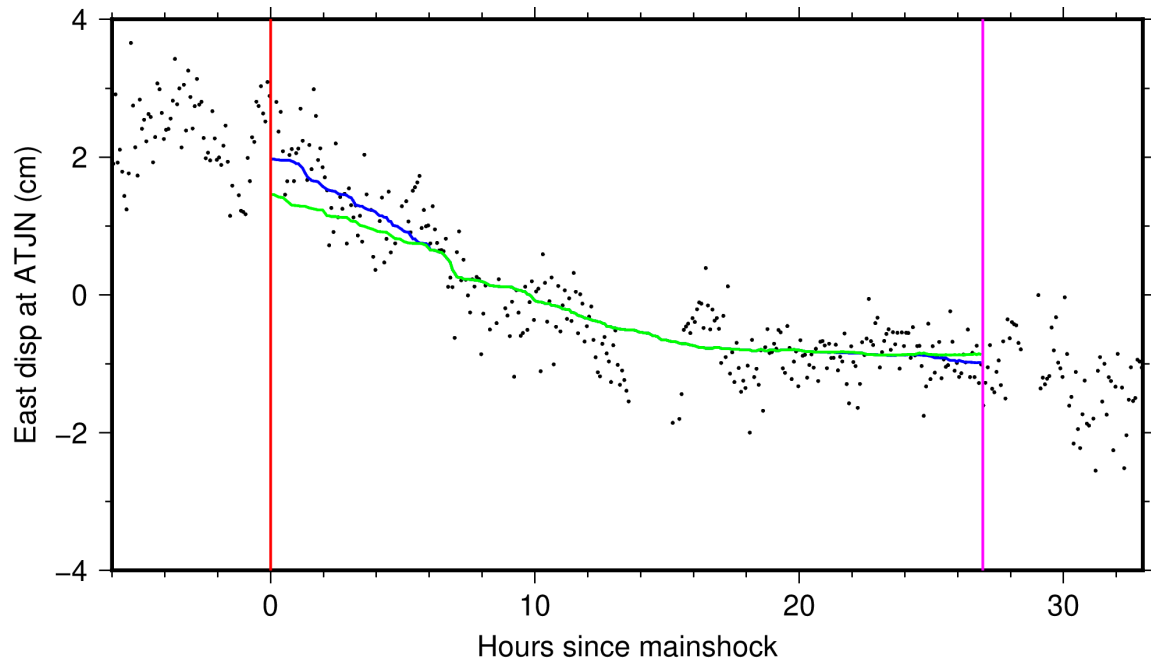


**Figure S22.** Comparison of moving median calculation with (blue) and without (green) data outside the interevent stage bounded by the mainshock (timing in red) and the largest aftershock (in magenta). The two coseismic steps (Figures S15a-b) are removed from the cleaned coordinates before calculating the moving median (black dots).

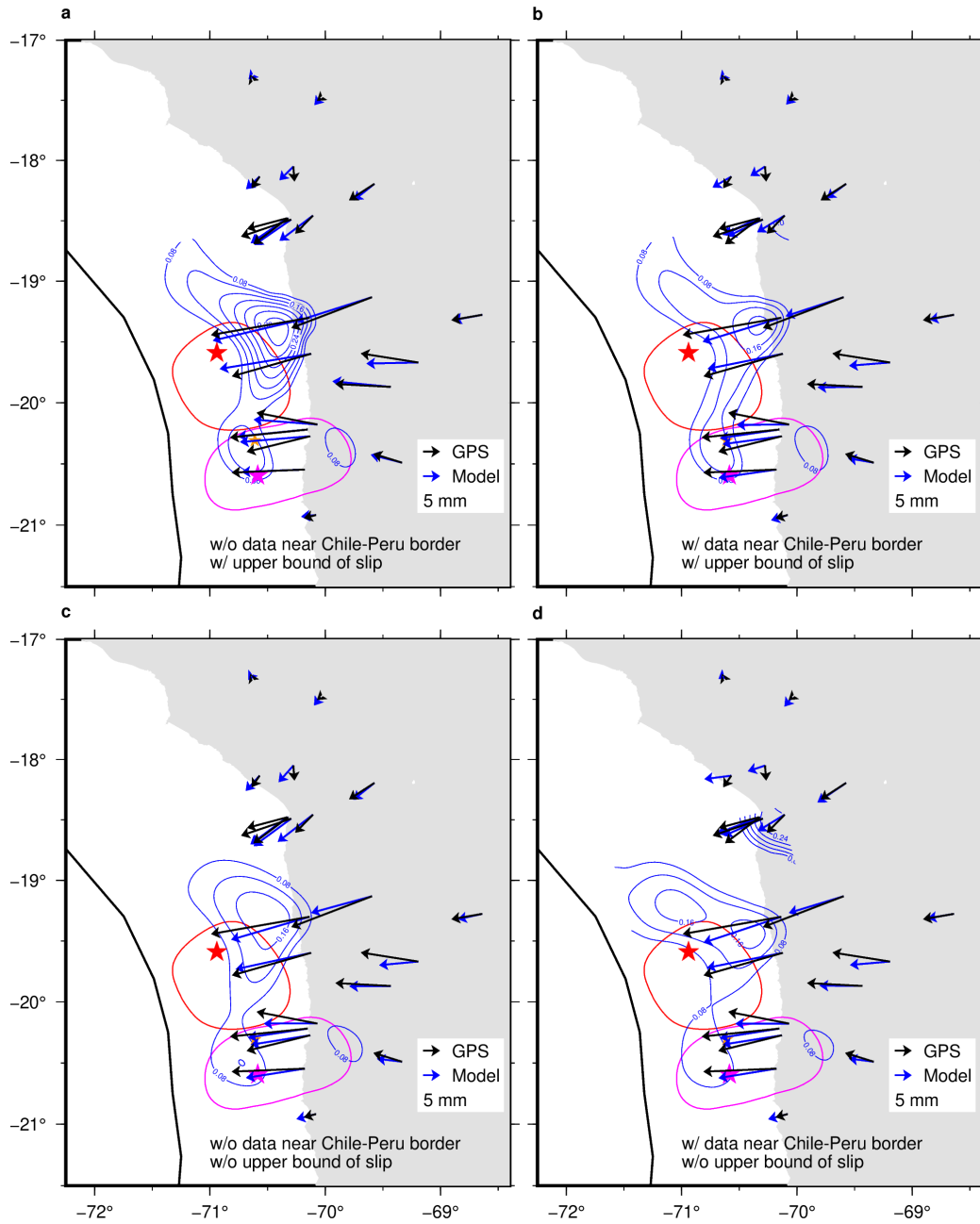


**Figure S23.** Slip inversions of the interevent cumulative displacement dataset derived from the moving median analysis (dataset (ii); See Text S4) with different settings. (a-b) The upper bound of slip amplitude (Figure 3a) is imposed and the data north of 19°S is included (a) or excluded (b). (c-d) The upper bound of slip amplitude is not imposed and the data north of 19°S is included (c) or excluded (d). See Figure 2e for other elements. Figure S23a is the same as Figure S17a.

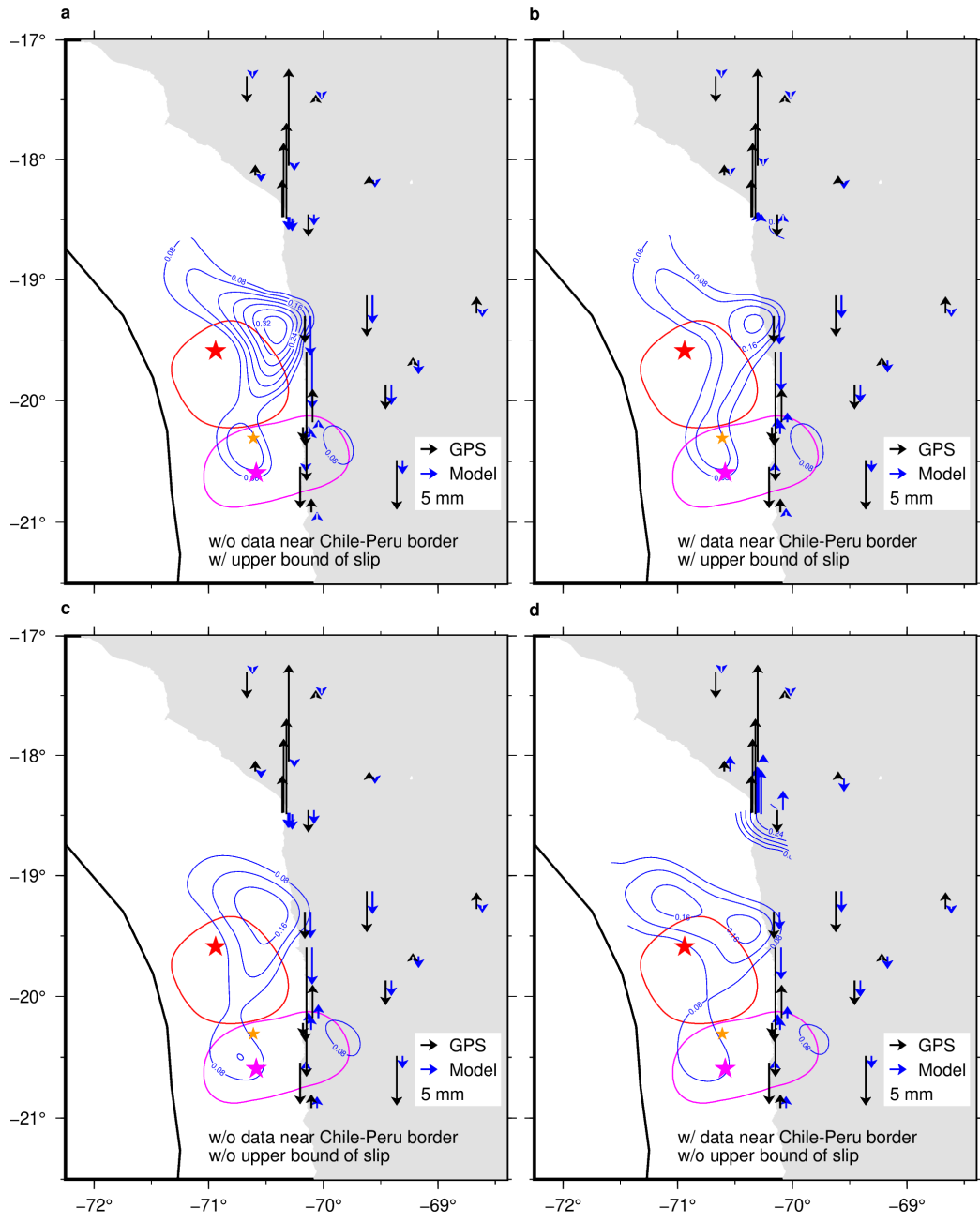


**Figure S24.** Same as Figure S23 but with the vertical data fit. Figure S24a is exactly same as Figure S17b.